High-resolution analyses of concentrations and sizes of refractory black carbon particles deposited on northwest Greenland over the past 350 years - Part 2. Seasonal and temporal trends in refractory black carbon originated from fossil fuel combustion and biomass burning

Kumiko Goto-Azuma[1,2], Yoshimi Ogawa-Tsukagawa[1], Kaori Fukuda[1], Koji Fujita[3], Motohiro Hirabayashi[1], Remi Dallmayr[1,a], Jun Ogata[1], Nobuhiro Moteki[4], Tatsuhiro Mori[5], Sho Ohata[3], Yutaka Kondo[1], Makoto Koike[6], Sumito Matoba[7], Moe Kadota[7], Akane Tsushima[1,b], Naoko Nagatsuka[1,c], and Teruo Aoki[1]

[1]National Institute of Polar Research, Tachikawa, Tokyo, 190-8518, Japan

[2]SOKENDAI, Shonan Village, Hayama, Kanagawa, 240-0193, Japan

[3]Nagoya University, Nagoya, 464-8601, Japan

[4]Tokyo Metropolitan University, Hachioji, Tokyo, 192-0397, Japan

[5]Keio University, Yokohama, Kanagawa, 223-8521, Japan

[6]University of Tokyo, Bunkyo-ku, Tokyo, 113-0033, Japan

[7]Hokkaido University, Sapporo, 060-0819, Japan

[a]Now at Alfred Wegener Institute for Polar and Marine Research, Bremerhaven, Germany

[b]Now at Nagasaki University, Nagasaki, 852-8521, Japan

[c]Now at Japan Agency for Marine-Earth Science and Technology, Yokosuka, Kanagawa, 237-061, Japan

Correspondence to: Kumiko Goto-Azuma (kumiko@nipr.ac.jp)

Abstract. The roles and impacts of refractory black carbon (rBC), an important aerosol species affecting Earth's radiation budget, are not well understood owing to lack of accurate long-term observations. To study the temporal changes in rBC since the pre-industrial period, we analysed rBC in an ice core drilled in northwest Greenland. Using an improved technique for rBC measurement and a continuous flow analysis system, we obtained accurate and high temporal resolution records of rBC particle size and mass/number concentrations for the past 350 years. Number and mass concentrations, which both started to increase in the 1870s associated with inflow of anthropogenically derived rBC, reached their maxima in the 1910s–1920s and then subsequently decreased.Backward trajectory analyses suggest that North America was likely the dominant source region of the anthropogenic rBC in the ice core. The increase in anthropogenic rBC shifted the annual concentration peaks of rBC from summer to winter–early spring. After rBC concentrations diminished to pre-industrial levels, the annual peak concentration of rBC returned to the summer. We found that anthropogenic rBC particles were larger than biomass burning rBC particles. By

separating the rBC in winter and summer, we reconstructed the temporal variations in rBC that originated from biomass burning, including the period with large anthropogenic input. The rBC that originated from biomass burning showed no trend of increase until the early 2000s. Finally, possible albedo reductions due to rBC are discussed. Our new data provide key information for validating aerosol and climate models, thereby supporting improved projections of future climate and environment.

1 Introduction

Black carbon (BC) particles, which are emitted by incomplete combustion of biomass and fossil fuels, affect Earth's radiation budget and thus climate (Bond et al., 2013; Moteki, 2023; Matsui et al., 2022; Legrand et al., 2016). In turn, changes in climate can affect emissions of BC from biomass burning through natural processes such as wildfires. Global warming is considered a major cause of the recent increase in large wildfires globally that can cause serious damage to ecosystems and human society (Calkin et al., 2023; Keeley and Syphard, 2021; Wang et al., 2021; Keane et al., 2008). Increased occurrence of large wildfires in the future could affect Earth's radiation budget, and change the frequency at which certain regions are exposed to serious hazard.Increases of fossil fuel combustion since the Industrial Revolution have changed Earth's radiation budget and contributed to the warming or cooling over the past century (Shindell and Faluvegi, 2009; McConnell et al., 2007; Breider et al., 2017). To understand the effects of BC on the radiation budget and the impact of climate change on BC emissions, the long-term changes in the concentrations and size distributions of BC particles should be   known. Data obtained since the pre-industrial period are particularly valuable because we cannot fully understand the anthropogenic effects without characterizing BC in a pristine environment. The Arctic is the key region for clearer elucidation of the roles of BC because the Arctic has warmed at a rate four times faster than that of the global average over the past half century, leading to drastic changes such as sea ice retreat, enhanced glacier mass loss, and ecosystem changes (Rantanen et al., 2022). Despite numerous studies based on observations and aerosol/climate models (e.g., Bond et al., 2013 and references therein), we have only limited knowledge on BC owing to lack of accurate long-term in situ observations (Mori et al., 2019). For the Arctic region, data are particularly sparse and few long-term records of BC size distribution exist.

Although there have been no direct observations before the past few decades, ice cores drilled in the Arctic have provided long-term records of BC. Development of the Single-Particle Soot Photometer (hereafter, SP2; Droplet Measurement Technologies, USA) (Stephens et al., 2003; Baumgardner et al., 2004) enabled measurements of refractory BC (rBC), the

2

58   terminology used for incandesce-based BC measurements (Petzold et al., 2013; Lim et al., 2014), in Arctic ice cores, where

59   BC concentrations are low and sample volumes are limited (McConnell et al., 2007; Zdanowicz et al., 2018; Zennaro et al.,

60   2014; Osmont et al., 2018). A continuous flow analysis (CFA) system is often used with the SP2 for high-resolution analysis

61   of ice cores (McConnell et al., 2007; Zdanowicz et al., 2018; Zennaro et al., 2014). With an SP2 attached to a CFA system,

62   McConnell et al. (2007) reconstructed rBC mass concentrations in central and southern Greenland since the pre-industrial

63   period. They showed that rBC concentration began a gradual rise after 1850, which was followed by rapid increase around

64   1890, a peak at around 1910, and then erratic decline through the late 1940s, followed by a sharp drop in the 1950s. They

65   attributed the increase to rBC derived mainly from fossil fuel combustion in North America. Similar anthropogenic temporal

66   trends have been reported for other Greenland sites (McConnell, 2010). The rBC flux records presented by McConnell (2010)

67   suggest that the anthropogenically derived increase in rBC was substantially less in northern Greenland than in southern

68   Greenland, which is closer to the emission sources in North America and Western Europe. McConnell et al. (2007) also

69   reported that the greatest increase in anthropogenic rBC occurs in winter. However, no rBC particle size data from Greenland

70   ice cores have been published to date.

71   At Arctic sites outside Greenland, only a few ice cores have been analysed for BC. An ice core from Holtedahlfonna

72   (Svalbard) indicated that BC mass concentration started to increase after 1850 and peaked around 1910, similar to the rBC

73   record of ice cores from Greenland (Ruppel et al., 2014). BC concentrations in the Holtedahlfonna core increased again

74   between 1970 and 2004, reaching unprecedented values in the 1990s. This increase is not seen in Greenland ice cores, and

75   contradicts atmospheric BC observations from Svalbard and other Arctic sites (Sharma et al., 2013), which indicate declining

76   concentrations of atmospheric BC. Ruppel et al. (2014) attributed the differences partly to the different sources of

77   anthropogenic BC affecting Svalbard and Greenland attributable to different air mass trajectories. They also suggested that

78   changes in scavenging efficiency might have affected the Holtedahlfonna BC record. An ice core from Lomonosovfonna,

79   another site in Svalbard (Osmont et al., 2018), showed gradual increase in rBC during 1800–1859, followed by dramatic

80   increase from 1860. The concentrations displayed two maxima at around 1870 and 1895, before they started to decline.

81   Between 1910 and 1949, concentrations of rBC were low. In contrast to the concentrations of rBC in Greenland, another

82   notable increase was evident in the Lomonosovfonna core after 1940, and the concentrations were at their highest in the 1950s

83   and 1960s. The rBC concentrations started to decrease in the 1970s, i.e., much later than the start of the decline in Greenland.

84   The authors argued that the differences between Greenland and Lomonosovfonna are partly related to the different source

85   regions of the air masses reaching Greenland and Svalbard.

86   The differences between the Holtedahlfonna and Lomonosovfonna records might also reflect different methods used

87   for the measurement of BC mass concentration. The samples from the Holtedahlfonna ice core were filtered, and then the

88   filters were analysed for BC using a thermal–optical method (Osmont et al., 2018), whereas the Lomonosovfonna and

89   Greenland ice cores were analysed using an SP2. Uncertainties regarding the filtering efficiency (Ruppel et al., 2014) and the

90   effects of dust particles on the thermal–optical method could partly explain the differences in the long-term trends in BC

91   concentrations. Furthermore, melt–freeze cycles that commonly occur at ice coring sites in Svalbard would have affected the

92   rBC concentrations (Osmont et al., 2018). Moreover, melt–freeze cycles could have agglomerated the rBC particles to larger

93   sizes beyond the detection range of an off-the-shelf SP2 (Osmont et al., 2018; Wendl et al., 2014). An ice core rBC record

94   from the Devon Ice Cap in the Canadian Arctic was also found to differ from the records of Greenland ice cores (Zdanowicz

95   et al., 2018). Although such differences could be partly attributable to different rBC source regions, melt–freeze cycles could

96   have also affected the Devon Ice Cap record. To investigate whether melt–freeze cycles did affect the derived BC

97   concentrations, we need to know the sizes of the rBC particles.

98   Even for ice cores drilled at sites where summer melting seldom occurs, such as those from interior Greenland, it is

99   important to investigate the size distributions of rBC particles to verify whether they are within the detection range of the SP2

100   instrument. This is because the sizes of rBC particles in snow are often larger than those in the atmosphere (Schwarz et al.,

101   2013; Mori et al., 2019) and exceed the detection range of a traditional SP2. The upper limit of detectable rBC diameter is

102   usually approximately 500 nm for the off-the-shelf SP2; that for SP2 modified by Moteki and Kondo (2010) is approximately

103   850 nm (Moteki and Kondo, 2010; Mori et al.,2019); and that for the off-the-shelf SP2 Extended Range (SP2-XR) is 800 nm.

104   If a large proportion of rBC particles have a diameter of >500 nm or 850 nm, the BC mass concentrations would be

105   underestimated (Mori et al., 2019; Goto-Azuma et al., 2024). Furthermore, if an ultrasonic nebulizer, such as the U5000AT

106   (CETAC Technologies, USA), was used with an off-the-shelf SP2, as was the case in most previous studies of rBC in ice cores

107   (McConnell et al., 2007; Kaspari et al., 2011; Zennaro et al., 2014; Bisiaux et al., 2012a, b; Wang et al., 2015; Zdanowicz et

108   al., 2018; Du et al., 2020), there would be large uncertainties in rBC mass concentrations (Wendl et al., 2014; Goto-Azuma et

109   al, 2024). Because the nebulizing efficiency of this type of nebulizer varies markedly for rBC particles < 850 nm (Ohata et al.,

110   2013; Mori et al., 2016; Goto-Azuma et al., 2024), variation in efficiency should be considered when calculating accurate mass

concentrations and size distributions (Ohata et al., 2013). However, this was not taken into account in most previous ice core studies. It is therefore important to analyse Arctic ice cores using an instrumental set-up that allows detection of rBC particles with diameter of >850 nm, and also to consider the size-dependent efficiency of the nebulizer. We developed a CFA system that includes an rBC unit, which allows accurate high-resolution measurement of concentrations and size distributions of rBC particles with diameter between 70 nm and 4 μm. Using this system, we analysed an ice core drilled at the SIGMA-D site in northwest Greenland. The details of this new system and its performance are described in the companion paper (Goto-Azuma et al., 2024). In this study, we analysed the data and investigated the temporal variability in concentration and size distribution of rBC that originated from fossil fuel combustion and biomass burning.

The BC detected in Arctic ice cores, together with NH_4^+ and specific organic materials (i.e., formate, levoglucosan, vanillic acid, and p-hydroxybenzoic acid), has been used to reconstruct past biomass burning (Ruppel et al., 2014; Zennaro et al., 2014; Grieman et al., 2017, 2018; Fischer et al., 2015; Pokhrel et al., 2020; Legrand et al., 2016). Although both BC and NH_4^+ have sources other than biomass burning (Osmont et al., 2018), levoglucosan, vanillic acid, and p-hydroxybenzoic acid primarily originate from biomass burning. However, the data regarding such organic materials usually have lower temporal resolution compared with that of rBC and NH_4^+ data owing to limitations of the measurement techniques. Furthermore, little is known about their changes during atmospheric transport and post-depositional processes (Hennigan et al., 2010). Different ice core proxies often show different temporal and spatial trends in biomass burning activities (Legrand and de Angelis, 1996; Legrand and Mayewski, 1997; Legrand et al., 1992, 2016; Kawamura et al., 2012; Grieman et al., 2017, 2018; Rubino et al., 2016; Zennaro et al., 2014). Compared with the Global Charcoal Database, which has been used widely to investigate changes in biomass burning on centennial to orbital time scales (Power et al., 2010; Marlon et al., 2016), ice core proxy records usually have higher temporal resolution. Even monthly or seasonally resolved continuous records of rBC and NH_4^+ for the past few centuries, millennia, and hundred thousand years have been derived from several Arctic ice cores, thereby allowing detection of high spikes in concentration in summer attributable to large boreal forest fires in northern North America and/or Siberia (Fischer et al., 2015; Zennaro et al., 2014). However, previous studies using rBC as a biomass burning tracer have been restricted to the pre-industrial period. This is because rBC originated from fossil fuel combustion contributed greatly to the total rBC concentrations and obscured the temporal trends in rBC related to biomass burning.

In this study, we reconstructed approximately monthly resolved concentrations and sizes of rBC particles in northwest Greenland over the past 350 years. The rBC originated both from biomass burning and from fossil fuel combustion was

138   distinguished owing to their different seasonal variability. In this paper, we discuss the temporal trends in the concentration

139   and size of rBC particles originated from both sources, and we investigate the rBC source regions based on backward trajectory

140   analyses. We then estimate the potential albedo reductions based on the monthly mean rBC concentration data.

141   **2 Materials and Methods**

142   **2.1 Ice core processing, analyses, and dating**

143   A 222.7 m ice core was drilled at the SIGMA-D site (77.636° N, 59.120° W; 2100 m a.s.l.; Fig. 1) in northwest Greenland in

144   spring 2014 (Matoba et al., 2015). The annual mean air temperature and accumulation rate at the site were estimated to be

145   −25.6 °C and 0.23 w eq a^{-1}, respectively (Nagatsuka et al., 2021). We examined the melt features (ice layers and thin crusts)

146   in the uppermost 20 meters of the SIGMA-D ice core, where increased summer melting would be expected due to recent

147   warming. We observed ice layers, with a maximum thickness of 10 mm, at only three depths. The 20-meter average melt

148   feature percentage (MFP) was 0.47%. The maximum MFP per meter was 1.7%, and 10 out of the 20 meters had no melt

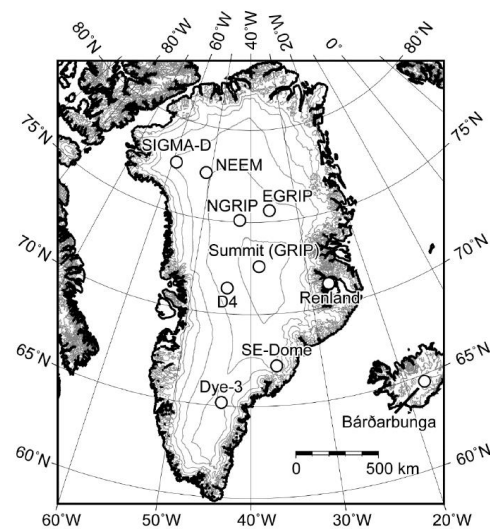149   features. Thus, the effects of melt-refreeze cycles are minimal at the SIGMA-D site.

Figure 1: Location of the SIGMA-D site and that of other drill sites.

150   The details of the ice core processing and analyses are described in the companion paper (Goto-Azuma et al., 2024);

151   therefore, we provide only a brief summary here. The top 175.77 m of the core was divided into two vertical sections (Sections

152   A and B) in the field. Section A was kept frozen and transported to the National Institute of Polar Research (NIPR) in Japan;

153   Section B was cut, melted, and bottled in the field.

154

Down to the depth of 112.87 m in Section A, we cut quadrangular prism samples with a cross section of 34 mm × 34 155

mm. For the depth interval between 6.17 and 112.87 m, we analysed rBC, stable isitopes of water, and six elements (i.e., ^{23}Na, 156

^{24}Mg, ^{27}Al, ^{39}K, ^{40}Ca, and ^{56}Fe) using the NIPR CFA system. The top 6.17 m of Section A was too fragile to be analysed using 157

the CFA system; hence, we manually cut it into segments of approximately 0.1 m. These "discrete samples" were 158

decontaminated in a −20 °C cold room using a precleaned ceramic knife and then placed in powder-free plastic bags. They 159

were then melted and transferred to precleaned glass and polypropylene bottles in a class 10,000 clean room. The samples in 160

glass bottles were analysed for stable isotopes of water and rBC. For the discrete samples, stable isotopes of water were 161

analysed using a near-infrared cavity ring-down spectrometer (L2120-i, Picarro Inc., USA), a high-precision vaporizer (A0211, 162

Picarro Inc., USA), and an autosampler (PAL HTC9 - xt - LEAP, LEAP Technologies, USA). The precision of determination 163

was ±0:05‰ for δ^{18}O. The samples in the polypropylene bottles were analysed for six elements (i.e., ^{23}Na, ^{24}Mg, ^{27}Al, ^{39}K, 164

^{40}Ca, and ^{56}Fe) using an inductively coupled plasma mass spectrometer (7700 ICP-MS, Agilent Technologies, USA) in a class 165

10,000 clean room at NIPR. 166

Both the CFA samples and the discrete samples were analysed for rBC using a Wide-Range SP2 (Mori et al., 2016), 167

which is a modified version of the SP2 (Droplet Measurement Technologies, USA), and a concentric pneumatic nebulizer 168

(Marin-5, Teldyne CETAC, USA). The combination of the Wide-Range SP2 and the pneumatic nebulizer enabled us to extend 169

the range of the size of rBC particles analysed (70 nm < diameter < 4 µm) to beyond those of the off-the-shelf SP2 (70 nm < 170

diameter < 500 nm) and the modified SP2 (Moteki and Kondo, 2010) or off-the-shelf SP2-XR (50-70 nm<diameter<800-850 171

nm). This combination and a careful calibration procedure enabled us to measure not only the concentration but also the 172

diameter of rBC particles. The analytical errors of the rBC mass and number concentrations were estimated to be <16% (Mori 173

et al., 2016; Goto-Azuma et al., 2024). The reproducibility of the rBC number and mass concentrations for repeated 174

measurements was usually better than 10% (Mori et al., 2019; Goto-Azuma et al., 2024). The detection limits of the rBC 175

number and mass concentrations were approximately 0.35 counts µL^{-1} and 0.02 µg L^{-1}, respectively. 176

Depths of Section B above 61.2 m were analysed for Na$^+$, K$^+$, Mg^{2+}, Ca^{2+}, Cl$^-$, NO$_3^-$, and SO$_4^{2-}$ using two ion 177

chromatographs (ICS-2100, Thermo Fisher Scientific, USA) at Hokkaido University (Japan), whereas depths between 61.2 178

and 112.87 m were analysed for NH$_4^+$, Na$^+$, K$^+$, Mg^{2+}, Ca^{2+}, Cl$^-$, NO$_3^-$, and SO$_4^{2-}$ using two ion chromatographs (ICS-2000, 179

Thermo Fisher Scientific, USA) at NIPR. The limit of detection of Na$^+$ measured at Hokkaido University was 10 µg L^{-1}, 180

181   whereas that measured at NIPR was 0.2 µg L^{-1}. Stable isotopes of water were analysed for all samples from Section B using

182   a near-infrared cavity ring-down spectrometer (L2130-i, Picarro, USA) and a high-throughput vaporizer (A0212, Picarro,

183   USA) at Hokkaido University. The precision of determination was ±0.1‰ for $\delta^{18}O$. For dating purposes, tritium concentrations

184   were measured using a liquid scintillation counter (LSC-LB3; Aloka Co. Ltd., Japan) at 0.05 m intervals for the depth interval

185   19.15–26.47 m (Nagatsuka et al., 2021).

186   Figure 2 shows the seasonal variability in Na and Na$^+$ concentrations, together with that in $\delta^{18}O$. Concentrations of

187   Na and Na$^+$ show maxima in winter and minima in summer, whereas the $\delta^{18}O$ shows maxima in summer and minima in winter

188   (Nagatsuka et al., 2021; Legrand and Mayewski, 1997; Mosher et al., 1993). We dated Section B of the SIGMA-D core by

189   annual layer counting using mainly Na$^+$ (Nagatsuka et al., 2021), which exhibited clearer seasonal variation compared to $\delta^{18}O$

190   and other ionic species The seasonal variation of $\delta^{18}O$, typically used for annual layer counting, was often obscured by diffusion

191   in the SIGMA-D core. However, we supplementarily used Ca^{2+} and $\delta^{18}O$ data when annual peaks of Na$^+$ were not clearly

192   observed. Additionally, we used a tritium peak (1963) and volcanic SO$_4^{2-}$ peaks (Katmai, 1912; Tambora, 1816, unknown,

193   1810; and Laki, 1783) as reference horizons, as reported by Nagatsuka et al. (2021). Because the CFA data from Section B

194   and the discrete data from Section A agreed well (Fig. 2), we basically adopted the chronology of Section B for that of Section

195   A with a few minor adjustments. The uncertainties of dating were estimated to be less than ±2 years. The CFA data covered

196   1653–2002, and the data from the top 6.17 m covered the period 2003–2013.

197   We divided one year into 12 months based on the assumption that the annual maxima and minima of Na$^+$

198   concentration correspond to 1 January and 1 July, respectively (Fig. 2). Each depth interval corresponding to a half year was

199   evenly divided into six months. Using the CFA data, we calculated the annual mean and the monthly mean values of the

200   number and mass concentrations of rBC particles. It is important to note that the months defined in this study may not align

201   exactly with calendar months for the following reasons: (1) precipitation is not evenly distributed throughout the year (Figs.

202   A1 and A2); (2) the minima and maxima of Na$^+$ concentrations do not necessarily coincide with 1 January and 1 July,

203   respectively; and (3) dry deposition would have a small contribution. As a result, there is inherent uncertainty in this definition.

204   The discrepancy between the "months" defined in this study and actual calendar months could be one or two months.

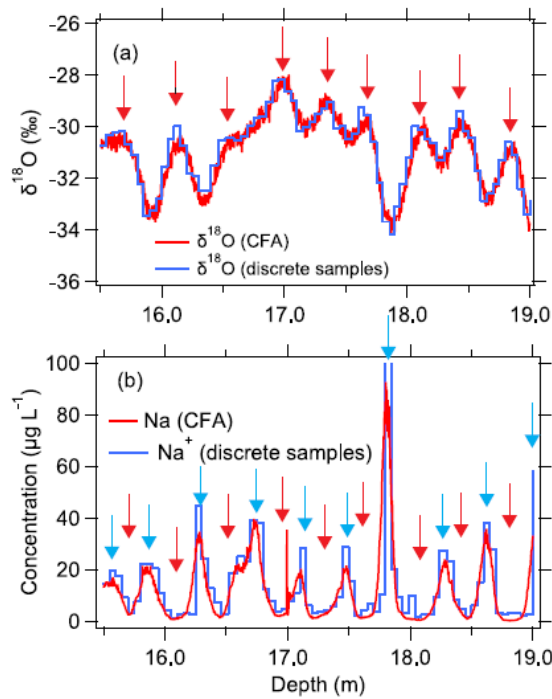205   Nevertheless, we will refer to these periods as "months" hereafter.

Figure 2: (a) $\delta^{18}O$ and (b) Na (and Na$^+$) concentrations. Red and blue curves represent data obtained from CFA measurements (this study) and discrete sample measurements (Nagatsuka et al., 2021) of the SIGMA-D core, respectively. Blue and red arrows indicate winter and summer, respectively. Winter and summer peaks were assumed to represent January 1 and July 1 of each year, respectively.

206   As demonstrated in the companion paper (Goto-Azuma et al., 2024), the dispersion lengths of the CFA system are

207   ~35 and ~39 mm for Na and BC, respectively. However, we could usually resolve two peaks which were 10 mm apart, although

208   the signal dispersion might slightly reduce the heights of the seasonal peaks.

209

210   **2.2 Backward trajectory analysis**

211   To estimate the contributions of different air masses affecting the SIGMA-D and D4 sites (Fig. 1), we performed 10-day

212   backward trajectory analyses for the period 1958–2015. Dividing the globe into 21 regions (Fig. A3), we calculated the

213   contribution from each region. We used the Single-Particle Lagrangian Integrated Trajectory (HySPLIT) model developed by

214   the National Oceanographic and Atmospheric Administration (NOAA) (Stein et al., 2015). The initial air mass was set at three

215   elevations at each site (i.e., 500, 1000, and 1500 m above ground level), and the accumulated probability of the air mass in

216   each 1° grid cell was calculated. Assuming wet deposition of rBC at the ice core sites, the air mass probability was weighted

217   with the local daily precipitation, i.e., if no precipitation occurred, the air mass was not considered, and vice versa. We used

218 ERA5 precipitation data produced by the European Centre for Medium-Range Weather Forecasts (Hersbach et al., 2020).

219 Details of the procedures are described in previous studies (Parvin et al., 2019; Nagatsuka et al., 2021).

220 For comparison, we also calculated the regional contributions without weighted for precipitation, while accounting for dry

221 deposition. However, we anticipate that dry deposition contributes only minimally compared to wet deposition (Appendix B).

222

223 **3 Results and Discussion**

224 **3.1 Impacts of anthropogenic emissions on long-term trends in concentrations and sizes of rBC particles**

225 Figure 3 displays annual and decadal averages of number and mass concentrations of rBC during the past 350 years. Notably,

226 monthly mean values could have been affected by the values of the adjacent one-two months, considering the resolution of the

227 CFA data (Sect. 2.1 and Goto-Azuma et al., 2024). Because we melted the core from the bottom to the top, the data for one-

228 two months after large rBC concentration peaks could have been affected. However, the annual and decadal averages were

229 unaffected by the CFA signal dispersion. We have also calculated annual rBC mass flux using annual mean rBC mass

230 concentration data and annual accumulation rate data (Fig.A4). Since there are no long-term trends in annual accumulation

231 rates, the temporal trends in rBC mass concentrations and rBC mass fluxes are consistent. Therefore, we used

232 concentration data in the following discussion.

233　　Many of the very high mass and number concentration peaks such as those in 1710 originated from large boreal forest

234 fires, as discussed in Sect. 3.3. Apart from these sporadic sharp peaks in number and mass concentrations, their background
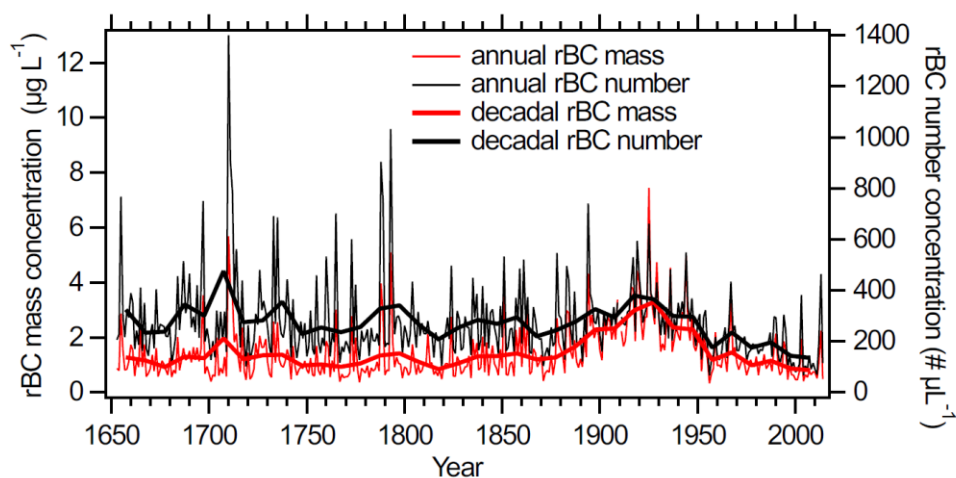

Figure 3: Annual mean (thin curves) and decadal mean (thick curves) concentrations of rBC. Red and black curves represent mass and number concentrations, respectively.

235 levels started to increase in the 1870s, reached their maxima in the 1910s–1920s, and decreased again since the 1930s.

236 Breakpoint analysis (Muggeo, 2003; de la Casa and Nasello, 2010) confirmed the timing of these increases and decreases. In

237 the 1960s, rBC number and mass concentrations returned to their pre-industrial levels. In the 1980s and 1990s, number

238 concentrations were below the pre-industrial level, whereas mass concentrations were similar to those of the pre-industrial

239 level. Before 1850, the major sources of rBC in Greenland were likely to have been biomass burning emissions from boreal

240 forest fires (Legrand et al., 2016; McConnell et al., 2007; Zennaro et al., 2014). The increases in rBC concentrations that

241 occurred in the late 19th century to mid-20th century are likely attributable to inflow to Greenland of rBC of anthropogenic

242 origin, as reported previously (McConnell, 2010; McConnell et al., 2007).

243   Direct comparison between the rBC concentrations in the SIGMA-D core and those in other Greenland ice cores is

244 not strictly feasible owing to methodological differences. rBC measurements in other Greenland ice cores were conducted

245 using the off-the-shelf SP2 coupled with an ultrasonic nebulizer (McConnell et al., 2007; McConnell, 2010; Zennaro et al.,

246 2014). This setup allows for the measurement of rBC particles with diameter of less than 500 nm (Goto-Azuma et al., 2024).

247 In contrast, the measurements of the SIGMA-D ice core could detect rBC particles with diameter up to 4 μm. Therefore, rBC

248 concentrations in other Greenland ice cores might have been underestimated during periods when the diameter of large

249 proportions of rBC particles exceeded approximately 500 nm. Owing to lack of information on size distributions, the extent of

250 the underestimation for other Greenland ice cores remains unknown. As described in the companion paper (Goto-Azuma et

251 al., 2024), if the off-the-shelf SP2 used in the previous studies had also been used for the SIGMA-D ice core, the extent of

252 underestimation would have depended on depth and hence on age. However, the general temporal trends in annual mean rBC

253 concentrations at the SIGMA-D site did not change notably if rBC particles with diameter of >500 nm, the maximum

254 measurable diameter of the off-the-shelf SP2, were excluded (Fig. 4). Therefore, it is informative to compare the rBC

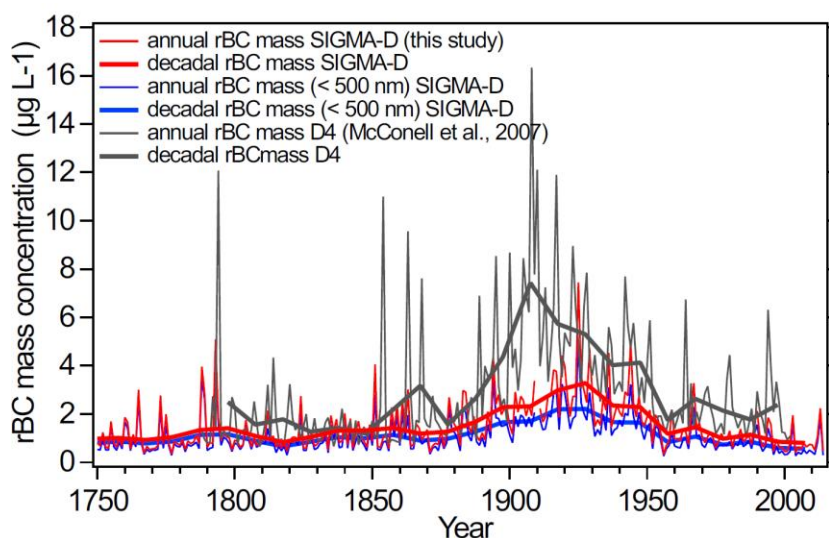255 concentration trends at the SIGMA-D site with those of other Greenland sites.

Figure 4: Annual mean (thin curves) and decadal mean (thick curves) mass concentrations of rBC. Red and black curves represent rBC concentrations at the SIGMA-D and D4 sites, respectively. Blue curves show rBC concentrations for rBC particles with diameter of <500 nm.

257   The long-term trends in rBC mass concentrations at the SIGMA-D site are broadly similar to those at other ice core

258   sites in Greenland (McConnell et al., 2007; McConnel., 2010), including the D4 site. However, the SIGMA-D core shows

259   much lower anthropogenic rBC concentrations, a later peak period, and later onset of the reductions in comparison with those

260   of the D4 core (Fig. 4). This is in accord with the studies by McConnel et al. (2007) and McConnel (2010), which indicate that

261   more southerly sites generally show higher anthropogenic rBC concentrations, an earlier peak period, and earlier onset of the

262   decline in anthropogenic rBC concentrations in comparison with those of more northerly sites. The BC emission inventories

263   for potential BC source regions indicate that emissions of anthropogenically derived BC started earlier in Europe than in North

264   America, and that the decline in anthropogenic BC concentrations started earlier in North America than in Europe or the former

265   USSR (Osmont et al., 2018). The emission inventories used by Osmont et al. (2018) were those adopted for the Coupled Model

266   Intercomparison Project phase 5 (CMIP 5; Bauer et al., 2013; Eckhardt et al., 2023; Lamarque et al., 2010). If those emission

267   inventories are reliable, then the slight difference in the temporal trends of rBC concentrations would indicate that southern

268   Greenland sites (e.g., the D4 site) had been influenced mainly by anthropogenic emissions from North America, whereas

269   northern Greenland sites (e.g., the SIGMA-D site) had been influenced by anthropogenic emissions from Europe and the

270   former USSR (in addition to those from North America), as was the case for anthropogenic sulphate (Goto-Azuma and Koerner,

271   2001). However, the results of our backward trajectory study do not support this hypothesis, as discussed below.

272   The 10-day precipitation-weighted backward trajectories for the SIGMA-D and D4 sites showed no contributions of

273   air masses from Antarctica (AT), Australia and New Zealand (AUS), South America (SAM), Southeast Asia (SEA), South

274   Asia (SA), the Antarctic Ocean (ATO), South Pacific Ocean (SPO), Indian Ocean (INO), and South Atlantic Ocean (SAO).

275   The four regions of the Middle East (ME), Africa (AF), East Asia (EA), and Central Asia (CA) (Fig. 5) showed maximum

276   contributions of <0.05%. In further analyses, we omitted the above 13 regions and focused on the eight regions of Europe

277   (EU), the Greenland Ice sheet (GrIS), Russia (RUS), North America (NA), the North Pacific Ocean (NPO), North Atlantic

278   Ocean (NAO), Arctic Ocean (AO), and Iceland (IC). Of these, GrIS, AO, NA, and NAO were found to be the major sources

279   of the air masses arriving at both the SIGMA-D site and the D4 site, although only NA represents a source of anthropogenic

280   BC emissions. Therefore, the temporal trends in anthropogenic rBC at both SIGMA-D and D4 appear to reflect the trend of
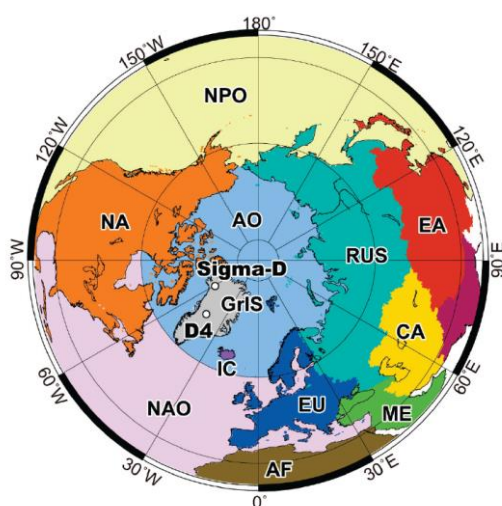
281   BC emission in NA.

Figure 5: The 12 regions showing non-zero contributions in precipitation-weighted backward trajectory analyses (GrIS: Greenland Ice Sheet, NA: North America, EU: Europe, RUS: Russia, CA: Central Asia, EA: East Asia, ME: Middle East, AF: Africa, NPO: North Pacific Ocean, NAO: North Atlantic Ocean, AO: Arctic Ocean, and IC: Iceland).

282   For precipitation-weighted trajectories, the contributions of air masses from EU and RUS, which are regions with

283   high levels of emission of anthropogenic BC (Hoesly et al., 2018), were less than 4% and 1%, respectively, at both the SIGMA-

284   D site and the D4 site, even in winter when their contributions are at their maxima. To investigate the influence of contributions

from EU and RUS in more detail, we recalculated the air mass contributions by excluding GrIS and the oceanic regions of

NPO, NAO, and AO where there are no sources ofBC emission. Although GrIS had the largest air mass contributions

throughout the year and throughout the 10 days, we excluded it because most of the region is covered with ice and has very

minor BC sources. The temporal variations in the contributions from NA, EU, RUS, and IC are plotted in Fig. 6 (for both

precipitation-weighted and unweighted trajectories), and the probability distributions of the air masses for the SIGMA-D and

D4 sites are displayed in Fig. 7 (for precipitation-weighted trajectories) and Fig. A5 (for precipitation-unweighted trajectories).

Except for the initial few days at D4, contributions from NA are the highest at both SIGMA-D and D4 sites for both

precipitation-weighed and unweighted trajectories throughout the year. The significant contributions of IC during the first few

days at the D4 site are likely due to its proximity to Greenland despite its small area, since IC is the only land region near

Greenland that can serve as a BC source region. However, if we include oceanic regions along with land regions, the
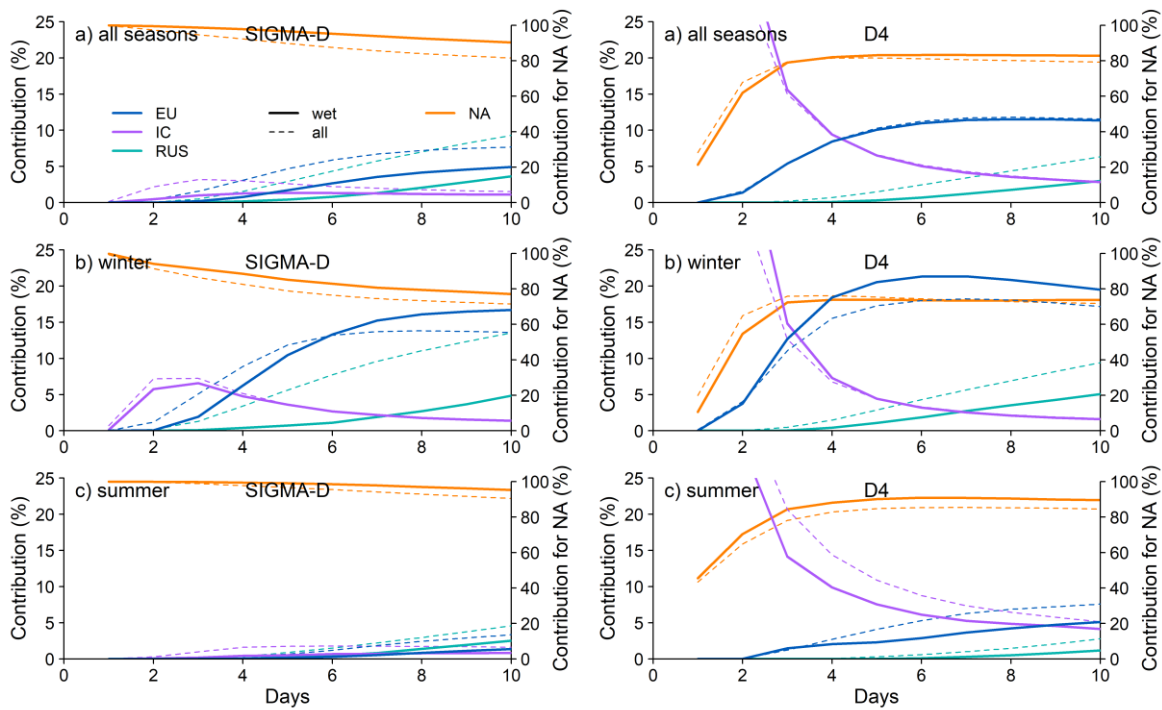
contribution from IC decreases substantially.

Figure 6: Temporal variability in contribution of air masses arriving at (left) the SIGMA-D site and (right) the D4 site from four regions: (a) averages of 12 months, (b) averages of winter months (December-February), and (c) averages of summer months (May-July). Right-hand axes indicate contributions from NA, and left-hand axes indicate contributions from the other regions. Solid and dashed curves denote results with and without weighing for the daily local precipitation, respectively.

14

296

297   At both SIGMA-D and D4 sites, the contributions from EU and RUS increase in winter (Figs. 6, 7, and A5) when air

298   masses from distant sources can more easily reach the Arctic (Jurányi et al., 2023) for both precipitation—weighted and

299   unweighted trajectories. Against our expectation based on CMIP 5 emission inventories, the contributions from EU were

300   slightly greater at D4 than at SIGMA-D. Although backward trajectory analyses showed that contributions from EU were

301   slightly different between the SIGMA-D and D4 sites, the results suggested the opposite conclusion to that of an assumption

302   based on the regional difference in emission inventories to explain the slight differences in the temporal trend of rBC at the

303   two sites. For precipitation-weighted trajectories, the contributions from RUS were similar at both sites and comprised

304   approximately 5% of the total at most in winter, when the anthropogenic input of rBC is greatest at both the SIGMA-D site

305   (see Sect 3.2) and the D4 site (McConnell et al., 2007). While precipitation-unweighted trajectories in winter show higher

306   contribution from RUS compared with precipitation-weighted trajectories at both SIGMA-D and D4 sites, the contribution

307   from RUS is greater at the SIGMA-D site than at the D4 site. The slight difference in temporal patterns of mass concentrations

308   of anthropogenic rBC between the two sites might reflect the different contributions from RUS in winter. However, it should

309   be noted that the 1958-2015 timeframe used for back trajectory calculations, a constraint given by availability of

310   reanalysis data, is not necessarily representative of the entire 350-year period. Nagatsuka et al. (2021), based on the back

311   trajectory studies for the SIGMA-D site, have shown that the interannual variability of contributions from different

312   regions remained relatively constant during 1958-2013. Thus, we can discuss the source regions of rBC for this period

313   based on our back trajectory calculations. For earlier periods, we can only hypothesize the back trajectories by assuming

314   similar atmospheric circulations to those of the 1958-2015 period. This could lead to large uncertainties for the years before
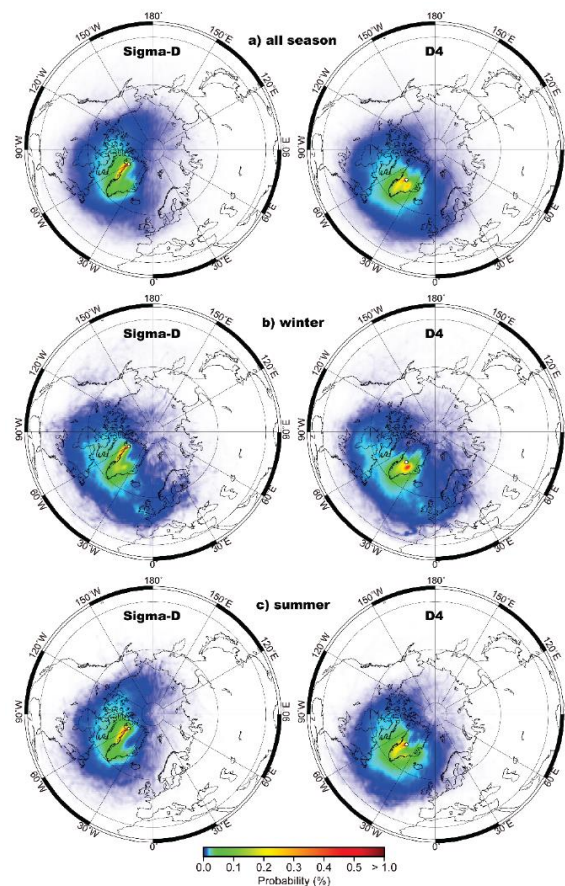
315   1958.

316

Figure 7: Probability distributions of air masses at (left) the SIGMA-D site and (right) the D4 site: (a) averages of all seasons, (b) averages of winter months (December–February), and (c) averages of summer months (May–July).

317   Additionally, there are large uncertainties in emission inventories. Although the CMIP 5 emission inventories appear

318   to reproduce the temporal patterns in concentrations and fluxes of rBC in Arctic ice cores better than those produced using the

319   Coupled Model Intercomparison Project phase 6 (CMIP 6) inventories, the reproduction of the magnitudes of the

320   concentrations and fluxes is better when using the CMIP 6 inventories (Eckhardt et al., 2023). A model intercomparison study,

321   which compared the modelling results obtained from 11 Earth System Models using CMIP 6 emission inventories with rBC

322   records from ice cores (Moseid et al., 2022), revealed errors in European emission inventories. However, the study also showed

323   that rBC concentrations in Northern Greenland ice cores reflected European emissions, contradicting our backward trajectory

324   analyses. It should be also noted that backward trajectory analyses are unable to capture the contributions of air masses

325   transported through the upper troposphere (Nagatsuka et al., 2021), which could be important when estimating the

326   contributions from distant sources. Currently, we are unable to explain the slightly different temporal trends in the rBC records

327   from different ice cores in Greenland. Further elucidation of this topic will require additional modelling studies constrained by

328   accurate rBC records from Greenland ice cores.

329   Figure 8 displays decadal mean mass and number size distributions of rBC for different periods with different

330   anthropogenic inputs. We assumed that the mass size distribution follows a lognormal distribution and thus we estimated the

331   mass median diameter (MMD), which is one of the measures of an rBC size distribution. The decadal mean MMD was 226

332   nm in the pre-industrial period of 1783–1792. It increased to 325 nm in the peak anthropogenic period of 1913–1922, and

333   subsequently decreased to 302 nm in 1993–2002 and 278 nm in 2003–2012. Number size distributions did not show noticeable

334   temporal change. To investigate the temporal changes in rBC size distribution, we used the average mass of rBC particles

335   (mBC) in addition to the MMD. The parameter mBC can be calculated by dividing the mass concentration by the number

336   concentration. Figure 9 shows the annual and decadal mean mBC and decadal mean MMD, together with the annual and

337   decadal mean rBC mass concentrations. Based on breakpoint analyses, we deduced the timing of rBC size changes. The annual

338   mean mBC and decadal mean mBC started to increase in the 1850s and the 1840s, respectively, while the decadal mean MMD
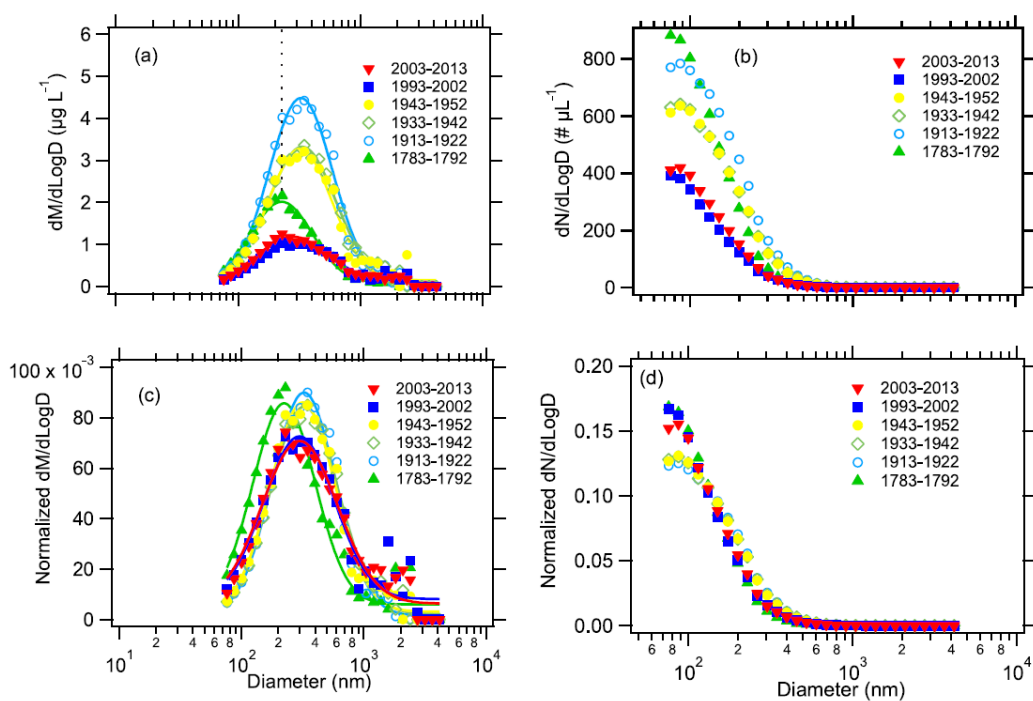

Figure 8: Temporal changes in decadal mean size distributions of rBC particles: (a) and (b) non-normalized mass and number size distributions, respectively, and (c) and (d) mass and number size distributions normalized by total rBC mass and number concentrations, respectively. Dotted line in (a) indicates the mass median diameter (MMD) for the period 1783–1792.
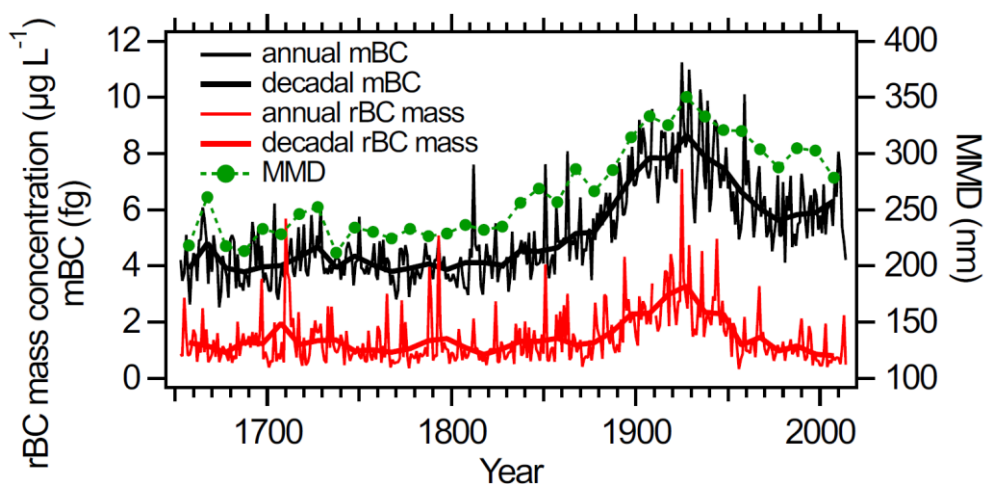
Figure 9: Annual and decadal mean mBC (black) and decadal mean MMD (green), together with annual and decadal mean rBC mass concentration (red). Thin and thick solid curves denote annual and decadal means, respectively.

339   started to increase in the 1820s. Annual mean mBC, decadal mean mBC, and decadal mean MMD peaked in the 1920s, when

340   the mass and number concentrations of rBC were at their maxima. The peak values of MMD and mBC were approximately

341   twice and 1.5 times, as high as the corresponding pre-industrial values, respectively. Anthropogenically derived rBC particles

342   that arrived in northwest Greenland appear to have been larger than rBC particles of biomass burning origin. This is contrary

343   to our expectation because it has been reported that the sizes of rBC particles from biomass burning are larger than those from

344   anthropogenic emissions near the sources (Bond et al., 2013). In the 1920s or 1930s, MMD and mBC both started to decrease,

345   as did the mass and number concentrations of rBC particles. However, in contrast to rBC concentrations, neither MMD nor

346   mBC returned to their pre-industrial levels; instead, they remained approximately 1.3 and 1.5 times higher than their pre-

347   industrial levels, respectively. We also notice that the start of the increases in mBC and MMD appear to have occurred earlier

348   than the increases in mass and number concentrations of rBC by 20–30 years.

349

350   **3.2 Temporal changes in seasonal variations in concentrations and sizes of rBC particles**

351   Figure 10 compares the monthly mean rBC mass concentrations in three periods: the pre-industrial period, the period with

352   high anthropogenic input, and recent years when concentrations decreased and returned to pre-industrial levels. Changes are

353   evident in the seasonality of rBC concentrations with respect to Na concentrations, which peak in winter. As reported by
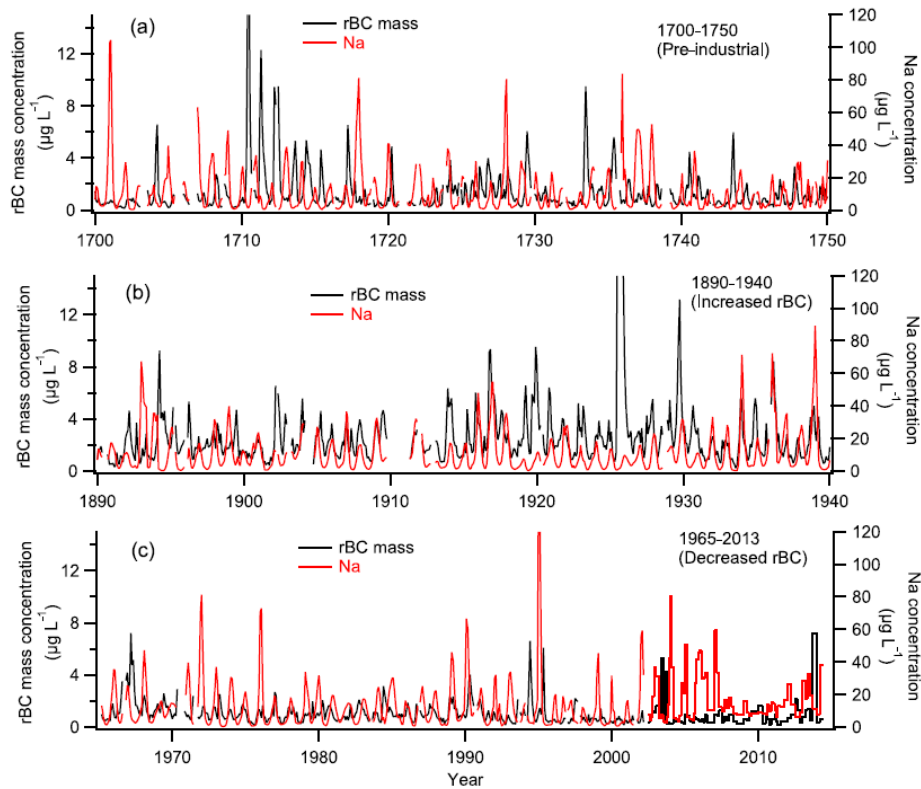
Figure 10: Monthly mean rBC mass concentrations and Na concentrations in three periods calculated from the CFA data, with the exception of 2003–2013 (concentrations for this period are raw data from the discrete samples that were analysed with monthly–bimonthly resolution).

354   McConnell et al. (2007) in relation to the D4 core, rBC concentrations peaked in summer in the pre-industrial period, whereas

355   they peaked in late-winter to early spring during the peak industrial period. Figure 10 also indicates that in recent years after

356   the rBC concentrations returned to their pre-industrial levels, the peaks once again occurred in summer. During the transition

357   period between the pre-industrial and the peak anthropogenic periods, and that between the peak anthropogenic period and

358   recent years, concentrations show complex seasonal variability. In some years, peaks occurred in both summer and winter/early

359   spring, whereas seasonal peaks were obscured or summer peaks and winter/early spring peaks appeared alternately in other

360   years.

361   To examine the general temporal trends in seasonal variations in rBC mass concentrations, we plotted 20-year

362   averages of rBC mass concentrations in each month for the years 1653–1992 and we plotted 10-year averages for 1993–2002

363   (Fig. 11). Up until the 20-year period of 1853–1872, rBC mass concentrations were elevated from March to September, peaking

364   in the late-spring to summer months (i.e., May–July). After the 20-year period of 1853–1872, rBC concentrations in autumn

to spring increased and became dominant. During the first half of the 20th century, rBC mass concentrations peaked in the

winter months of December and January. The autumn to spring increases in rBC concentrations are likely attributable to inflow

of anthropogenic emissions (McConnell et al., 2007). The seasonality of the anthropogenic rBC at SIGMA-D is consistent

with that of the present-day atmospheric rBC observations at Arctic sites such as Alert (Canadian high Arctic), Ny-Alesund

(Svalbard), Barrow (Alaska), and a Greenland coastal site (Sharma et al., 2006, 2019; Gong et al., 2010; Qi and Wang, 2019;

Massling et al., 2015).

After the 20-year period of 1913–1933, when the anthropogenic input was at its maximum, the autumn to spring
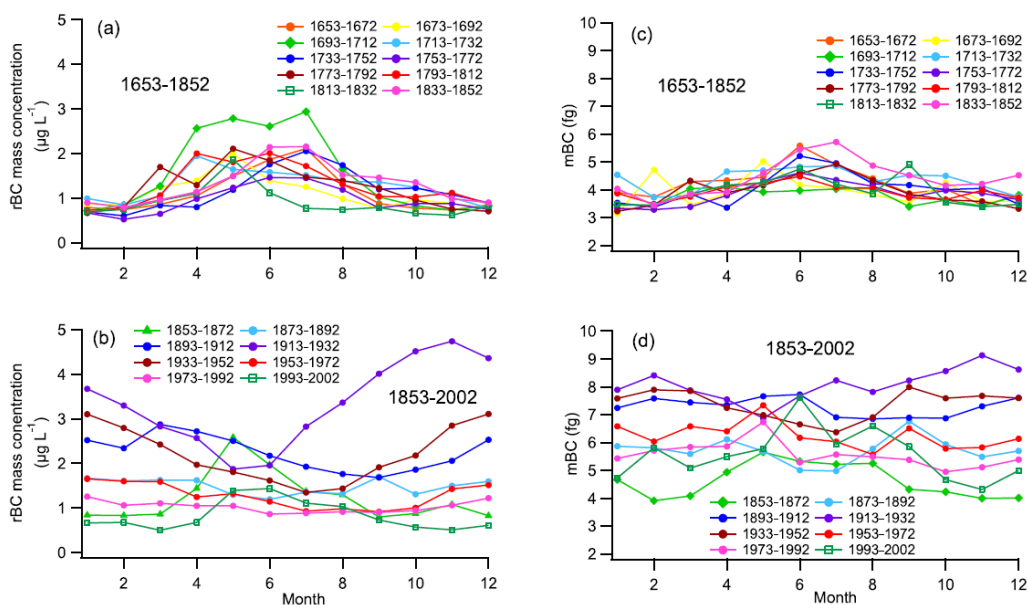

Figure 11: Twenty-year averages of (a) and (b) rBC mass concentrations and (c) and (d) mBC in each month for the years 1653–1992 and the 10-year averages for 1993–2002.

concentrations decreased. During 1993–2002, the rBC mass concentration peaked in summer again. The recent seasonality of

rBC at the SIGMA-D site is the same as that observed at other Greenland ice-coring sites, including EGRIP (Du et al., 2020)

and Summit (Fig. 1) (Schmeisser et al., 2018), but it differs from that of atmospheric observations in the Arctic (including

Greenland), where rBC concentrations peak in winter/early spring (Sharma et al., 2006, 2019; Gong et al., 2010; Qi and Wang,

2019; Massling et al., 2015). Although we do not present the results for rBC number concentrations, they showed seasonal

variations similar to those found in mass concentrations. The influence of anthropogenic emissions in the recent two decades

appears to be much lower at the ice coring sites of SIGMA-D, EGRIP, and Summit, located at elevations of >2000 m a.s.l., in

379   comparison with that at atmospheric observation sites located near sea level where anthropogenic emissions remain dominant.

380   At the high-elevation sites on the GrIS, concentrations of rBC from biomass burning have exceeded those associated with

381   anthropogenic emissions since the late 20th century, which is likely attributable to reduced emissions of anthropogenically

382   derived rBC, primarily in NA and secondarily in EU (McConnell, 2010; McConnell et al., 2007; Moseid et al., 2022).

383   To understand the general temporal trends in seasonal variations in rBC size, we plotted 20-year averages of mBC

384   in each month for the years of 1653–1992 and we plotted 10-year averages for 1993–2002 (Fig. 11). Up until the 20-year

385   period of 1853–1872, mBC peaked in spring to the summer months (May–July) in most of the 20-year periods and it never

386   peaked in the winter months. After the 20-year period of 1853–1872, mBC in autumn–spring increased, and its seasonality

387   became obscured. After the peak anthropogenic period of 1913–1933, mBC in autumn–spring decreased. During 1993–2002,

388   mBC once again peaked in summer. We see similar temporal trends in Figs. 12 and 13, i.e., both MMD and mBC showed

389   higher values in summer in the pre-industrial period. This seasonality would indicate that the sizes of rBC particles originated

390   from biomass burning are greater in summer than in winter. The winter and summer mBC started to increase in the 1820s–

391   1830s with a larger rate of increase for winter mBC. Winter and summer values both peaked in the 1890s–19430s and

392   subsequently decreased, with a larger rate of decrease for winter. The winter and summer MMD started to increase in the

393   1840s and 1810s, respectively, with larger rate of increase for winter MMD. While winter MMD started to decrease in the

394   1900s – 1920s and has continued to decrease, the summer MMD did not exhibit a clear downward trend. During the peak

395   anthropogenic period, the summer and winter mBC and MMD were close, which obscured the seasonality in rBC particle size

396   (Fig. 11). We also note that during the peak anthropogenic period, rBC particles larger than 1 μm in diameter increased in

397   winter (Fig. 13). The winter values of MMD and mBC became lower than the summer values in 1993–2002. Larger rBC

398   particles in winter in the anthropogenic period support the argument that rBC particles deposited at SIGMA-D were larger

399   when originating from anthropogenic emissions than when associated with biomass burning.

400   In the pre-industrial period, biomass burning would have been the predominant source of rBC. Backward trajectory

401   analyses (Figs. 6, 7, and A5) indicate that boreal forest fires in NA would be the primary sources of rBC in summer at both

402   the SIGMA-D site and the D4 site. Although the contributions of air masses from RUS are very small, especially in summer

403   (<3% at SIGMA-D; <1% at D4 for precipitation-weighted trajectories), Siberia has also been proposed as a potential source

404   of pyrogenic aerosols to Greenland (Zennaro et al., 2014). A recent study using the CAM-ATRAS global climate–aerosol

405   model (Matsui et al., 2022) showed that Siberia has made the largest contribution to rBC concentrations found in the recent
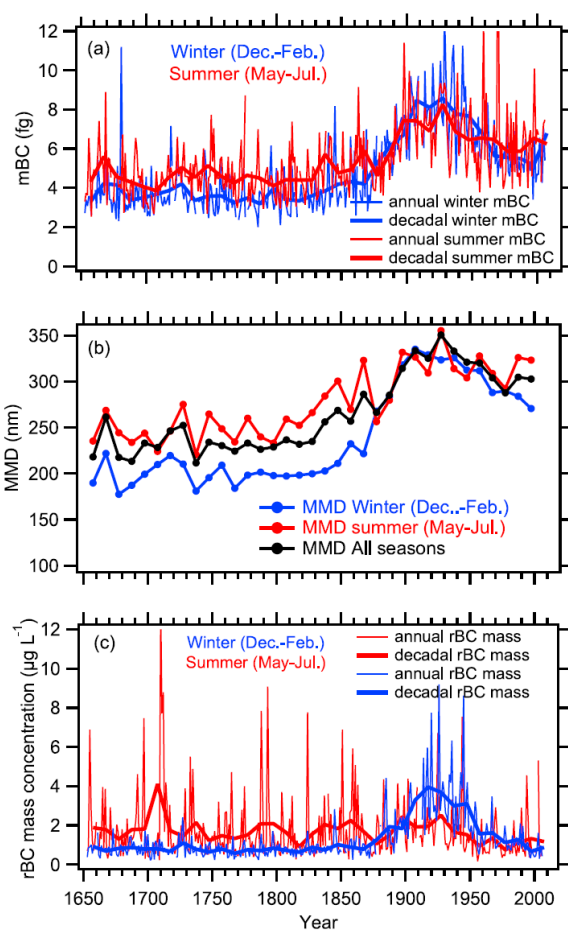
Figure 12: (a) Annual and decadal means of winter (December–February) and summer (May–July) mBC, (b) decadal means of winter, summer, and all-season (January–December) MMD, and (c) annual and decadal means of winter and summer rBC mass concentrations. In all panels, thin and thick solid lines denote annual and decadal means, respectively. Blue, red, and black curves denote winter, summer, and all-season means, respectively.

406   Arctic snow, although the contribution to Greenland snow specifically has not been reported. Therefore, Siberia could be a

407   secondary source of rBC at the SIGMA-D site in summer. In winter, the boreal forests in NA and Siberia are covered with

408   snow and thus there is little contribution of BC from boreal forest fires (Bond et al., 2013). However, rBC concentrations are

409   not zero, even in winter. Biomass burning in lower latitudes (Zennaro et al., 2014) could be a source of rBC in winter, and the

410   smaller sizes of rBC particles in pre-industrial winter periods suggest long-range transport of rBC that supports this assumption.
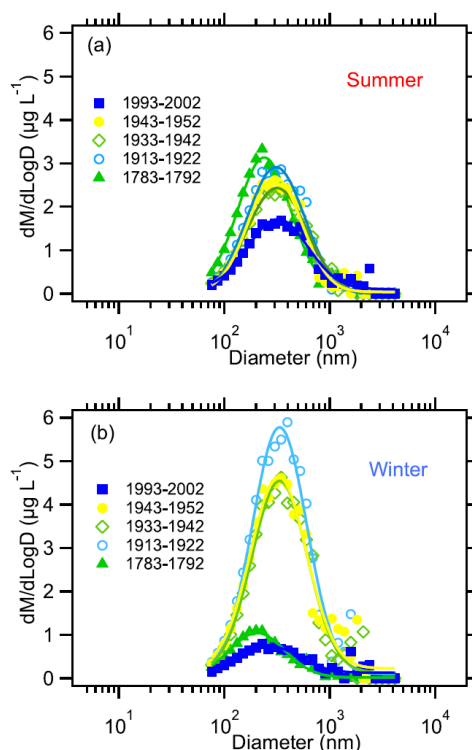
Figure 13: Temporal variability in mass size distributions of rBC particles during (a) winter (December–February) and (b) summer (May-July).

3.3 Historical changes in rBC originated from biomass burning

Figure 14 presents monthly mean rBC mass concentrations for the past 350 years, together with NH_4^+ concentrations. Occasional high peaks in summer, which lasted for one-two months, likely originated from large boreal forest fires, mainly in NA but with possible additional contributions from Siberia. Many of the high rBC peaks in summer coincide with high NH_4^+ concentration peaks in summer, which originate from large boreal forest fires (e.g., Legrand et al., 2016). Table A1 lists the biomass burning events distinguished in the record of the SIGMA-D ice core, and in other ice cores and the surface snow of Greenland. The events distinguished in the SIGMA-D core were defined using rBC mass concentration peaks and NH_4^+ concentration peaks. For rBC, peaks exceeding the summer (May–July) averages for 350 years + 2σ or 3σ were selected, whereas for NH_4^+, summer peaks exceeding the annual averages for 350 years + 2σ or 3σ were selected. If an rBC or NH_4^+ summer peak in the SIGMA-D core with a concentration between the average + 1σ and 2σ was found in the same year as when a large biomass burning event was recorded at other Greenland sites, we also selected that peak as a biomass burning event. If the year of a biomass burning event reported by previous studies agreed with that in the SIGMA-D core to within ±2 years, taking account of dating errors in different ice cores, we assumed that the record in the different cores reflected the same event.

424   In Fig. 14(b), we marked only those events exceeding the average + 3σ. Most of the marked events (peaks in 1655, 1665, 1697,

425   1710, 1711, 1712, 1733, 1788, 1793, 1824, 1851, 1859, 1863, 1925, and 1944) occurred in May, June, or July; however, those

426   in 1789, 1812, and 1894 occurred in April, the one in 1773 occurred in September, and the one in 1929 occurred in September-

427   October. The peak in 1925 occurred in July-August, and that in 1944 occurred in May and June, and we assumed that they

428   originated from large biomass burning events. Nevertheless, we could not abandon the possibility that these summer peaks

429   might have been affected by large peaks in the preceding winters owing to signal dispersion in the CFA system.

430   Most of the large events with rBC concentrations that exceeded the average + 3σ were also recorded in boreal forest

431   fire records reconstructed from rBC, NH_4^+, or levoglucosan concentrations in other Greenland ice cores (Table A1). The high

432   rBC concentration peaks in the summers of 1665, 1710, 1711, 1712, 1812, and 1824, accompanying high NH_4^+ peaks, and the

433   high rBC peak in 1859 have not been reported previously. The high NH_4^+ concentration peaks in 1675, 1690, and 1750 have

434   no corresponding rBC peaks in April, May, June, July, or August, while those in 1697, 1710, 1712, 1715, and 1761 do have

435   corresponding rBC peaks. As for the NH_4^+ concentration peak in 1690, the summer rBC data were missing and therefore

436   comparison was not possible. Although Keegan et al. (2014) argued that the high summer rBC concentrations in 1889 and

437   2012 found at Summit were associated with widespread melt events in Greenland, no high rBC concentration peaks were

438   found in 1889 or 2012 at the SIGMA-D site. As shown in Fig. 14 and Table A1, some of the large biomass burning events
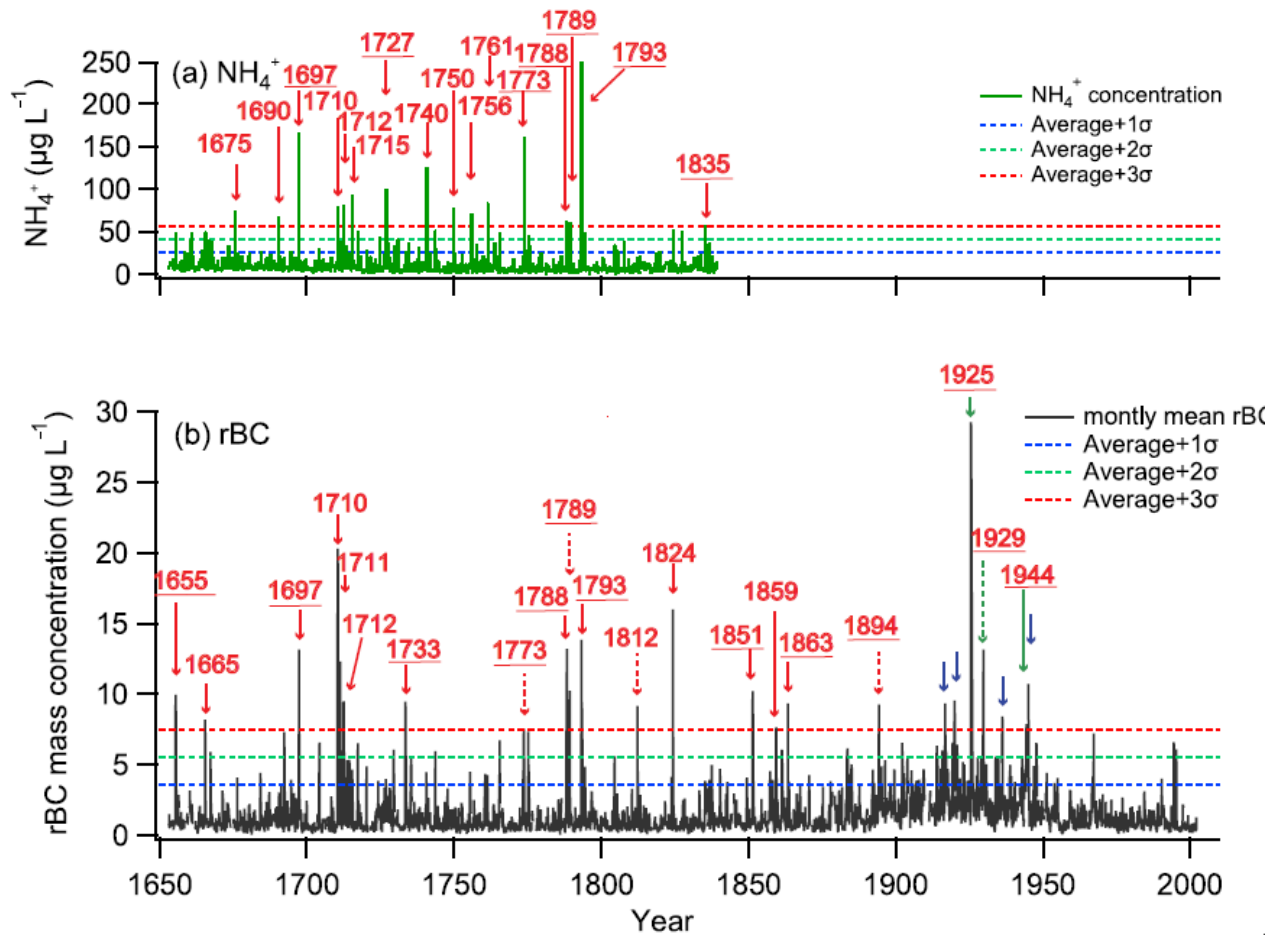
Figure 14: (a) NH₄⁺ concentrations: (raw data, and (b) monthly mean rBC mass concentrations (calculated from CFA data. Red arrows in (a) show years when concentrations exceeded the average + 3σ in summer. Solid and broken arrows in (b) show years when concentrations exceeded the summer (May–July) average + 3σ in summer (May–July), and in spring or autumn months (April, August, and September), respectively. Blue arrows in (b) show years when concentrations exceeded the summer average + 3σ in winter. Solid and broken green arrows in (b) show years when concentrations exceeded the summer (May–July) average + 3σ in summer (May–July), and in spring or autumn months (April, August, and September), respectively, but those that might have been affected by winter peaks. Underlining denotes years when biomass burning events were also recorded in other Greenland ice cores/surface snow samples within 2 years. Dotted lines in (a) denote the concentration average over 350 years + 1σ (blue), + 2σ (green), and +3σ (red). Dotted lines in (b) denote summer (May–July) concentration average over 350 years + 1σ (blue), + 2σ (green), and +3σ (red).

439 recorded in other Greenland ice cores were not recorded in the SIGMA-D core, and vice versa. There are two possible reasons

440 for this: (1) different ice core sites are not always on the transport pathways of rBC from boreal forest fires (Legrand et al.,

441 2016), and (2) wind scour at a site can remove snow containing high concentrations of rBC. Despite the minor regional

442 differences within Greenland, most of the large rBC concentration peaks caused by large biomass burning events were recorded

443 widely across Greenland. This indicates that high rBC concentration peaks could be used to synchronize different ice cores in

444 Greenland as reference horizons for dating, as is usually carried out with volcanic sulphate peaks and their signatures detected

445 by DEP(dielectric profiling) and ECM (electrical conductivity measurement) peaks (Rasmussen et al., 2008; Sinnl et al., 2022).

446   The numbers of large biomass burning events in each 10 years are plotted in Fig. 15 using different definitions of a

447 "large" event. Figure 15(a) displays the numbers of months with mass concentrations in summer (May–July) exceeding the

448 summer average + 1σ, 2σ, and 3σ; Fig. 15(b) displays the number of months with number concentrations in summer exceeding

449 the summer average + 1σ, 2σ, and 3σ. Because large events in April, August, and September were not counted to avoid the

450 potential for impact of anthropogenic rBC, there would be minor underestimation of the number of large events. Although the
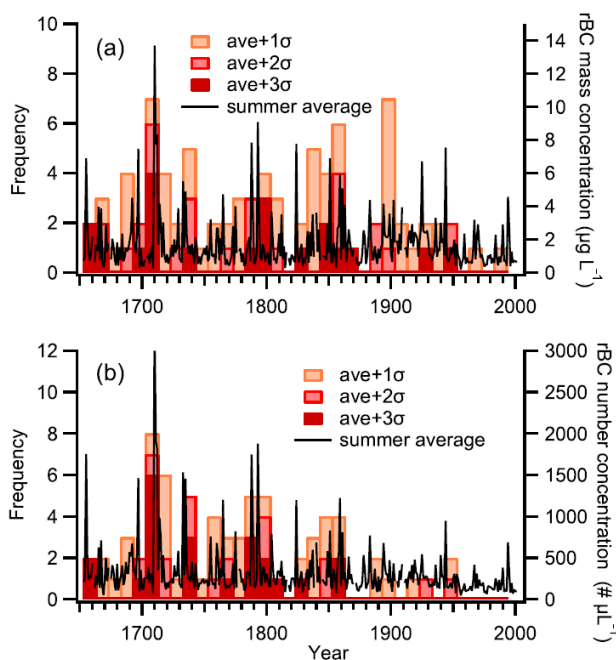
Figure 15: Frequency of large biomass burning events. Black curves denote summer (May–July) averages of rBC concentrations. Bars show frequency of rBC summer peaks in each decade exceeding the average + 1σ, 2σ, and 3σ. (a) Mass concentrations of rBC were used to define peaks. (b) Number concentrations of rBC were used to define peaks.

451 frequency of large events differs slightly between the different definitions, the general tendency is consistent. Large events

452 tended to be more frequent around the 1710s, 1790s, 1850s, 1900s, and 1950s. Moreover, there is no obvious trend of increase

up to the decade 1993–2002. To study the historical trends in concentrations of rBC originated from biomass burning, we calculated the decadal averages of rBC mass and number concentrations for each month (Fig. 16). During the pre-industrial period, both mass and number concentrations were stable in the winter months (December–February), whereas they showed large inter-decadal fluctuations in spring to autumn months (March–November). The fluctuations appear largest in spring–
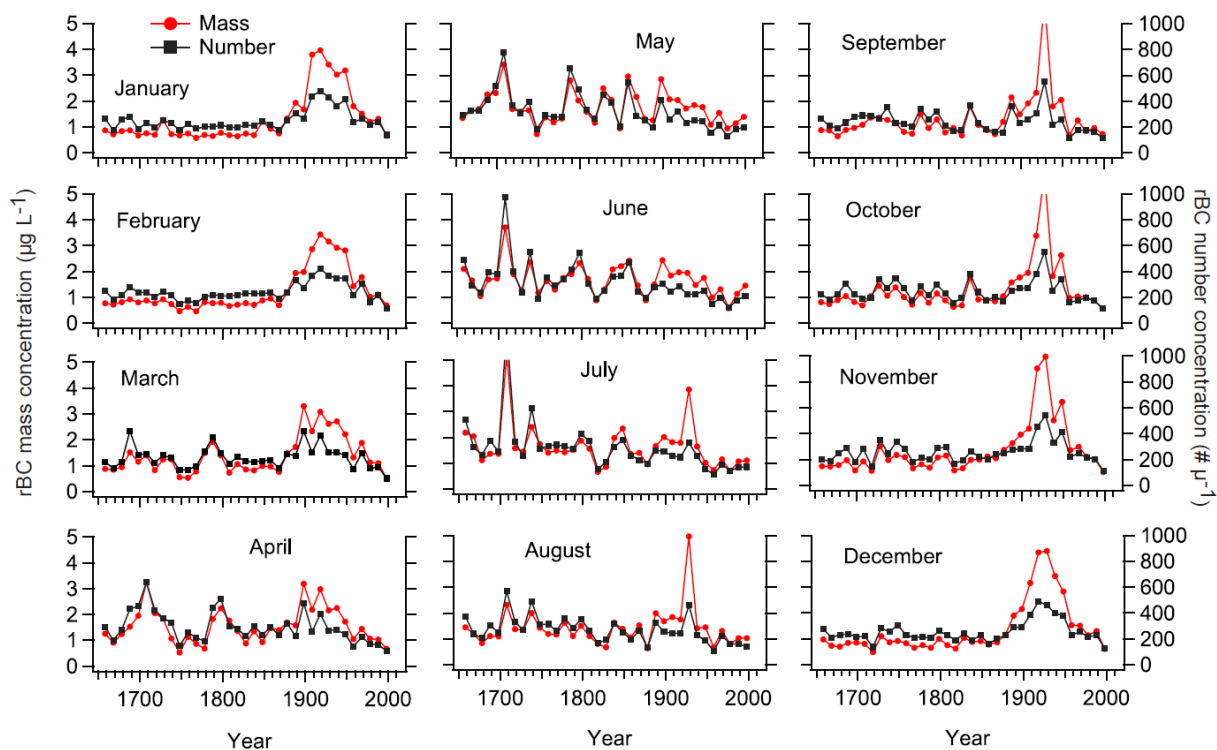

Figure 16: Decadal averages of rBC mass (red) and number (black) concentrations for each month.

summer (April–July). Generally, the period of April–July is likely when the occurrence of large boreal forest fires increases in NA (Whitman et al., 2018). The sporadic nature of the frequency of occurrence of large boreal forest fires would explain the large fluctuations.

Since the 1870s, when anthropogenic rBC started to influence the SIGMA-D site, rBC mass and number concentrations in September–April increased, as discussed in Sect. 3.2; however, there was little increase during the spring–summer months. The same feature is also seen in Fig. 12(c). Although large inter-decadal variability in concentrations during spring–summer obscured the temporal trends in spring–summer concentrations (Fig. 11), the general temporal trends are more apparent in Fig. 16. At the SIGMA-D site, we see slight trends of reduction in rBC mass and number concentrations during spring–summer. Analysis of Fig. 15 also suggests that the frequency of large boreal forest fires in NA showed a slight trend

466   of reduction over the past 350 years until the most recent decade (1993–2002). However, this trend has not been reported by

467   previous studies on other ice cores from Greenland, partly owing to the different periods covered, the different temporal

468   resolution of the analysis methods, and the different fire proxies used (Zennaro et al., 2014; Legrand et al., 2016; Parvin et al.,

469   2019; Savarino and Legrand, 1998; Whitlow et al., 1994). Most previous studies used NH_4^+ as a fire proxy, with occasional

470   use of levoglucosan and other organic materials; only a few studies have used rBC as a fire proxy for pre-industrial periods

471   (Zennaro et al., 2014).

472   Since the 1950s, data on the area burned and the number of forest fires in Canada have become available (Hanes et

473   al., 2018; Skakun et al., 2021). The SIGMA-D record does not appear to trace the Canadian forest fire database. Air masses

474   arriving at the SIGMA-D site might not have passed over Canada during periods of large forest fires. Large uncertainties in

475   fire data might also explain the disagreement. There are also large uncertainties and regional variability in sedimentary charcoal

476   fire records (Marlon et al., 2012, 2013; Power et al., 2013). However, our results are consistent with the charcoal data from

477   western NA, which show general decline in biomass burning since 1500, with a relatively enhanced fire period in the mid-19th

478   century (Power et al., 2013). The biomass burning emission inventories for CMIP 6 also have large uncertainties (van Marle

479   et al., 2017). Therefore, much more work is needed on the reconstruction of past biomass burning using ice cores.

480

481   **3.4 Impacts of rBC on the ice sheet albedo**

482   McConnell et al. (2007) calculated the quantitative impacts of rBC in snow on radiative forcing during early summer using

483   rBC concentration from D4 ice core and the Snow, Ice, and Aerosol Radiative (SNICAR) model (Flanner et al., 2007),

484   assuming an effective snow grain radius of 100 μm. They estimated the radiative forcing of 1.02 Wm^{-2} during the peak 5-year

485   period from 1906 to 1910, representing a fivefold increase compared to   preindustrial conditions. However, the radiative

486   forcing of rBC in snow varies depending on both the assumed solar irradiance and snow grain size. In this study, we calculated

487   the possible albedo reduction due to rBC at the SIGMA-D site from the monthly mean rBC mass concentration data obtained

488   in this study (Fig. 17) using a physically based snow albedo model (Aoki et al., 2011). As the snow albedo reduction rate due

489   to light absorbing particles is enhanced with an increase of snow grain size (Wiscombe and Warren, 1980), we assumed two

490   effective snow grain radii $r_s = 50$ μm and 1000 μm, corresponding to new snow (defined as " precipitation particles " according

491   to Fierz et al., 2009) and old melting snow (defined as " melt forms " according to Fierz et al., 2009) (Wiscombe and Warren,

492   1980) for clear sky and cloudy sky (overcast) conditions. The albedo reductions under the cloudy sky are 20-48% larger than

493   those under clear sky. These increases are related to the following two factors: (1) the visible albedo depends on rBC

494   concentration more strongly than the near infrared albedo (Wiscombe and Warren, 1980); (2) the visible spectral fraction in

495   solar irradiance at the snow surface under cloudy sky is larger than that under clear sky (Aoki et al., 1999). Thus, the albedo

496   reduction due to rBC under cloudy sky is enhanced more than clear sky.

497   Figure 17 demonstrates that the albedo reduction in case of new snow is consistently less than 0.01, even at the

498   maximum value for cloudy conditions in August 1925 (Fig. 17a). In contrast, for old melting snow, the albedo reduction

499   frequently exceeds 0.01 for both sky conditions (Fig. 17b). The maximum albedo reduction for cloudy conditions is 0.045 (r_s

500   = 1000 μm) and 0.0098 (r_s = 50 μm) in August 1925, followed by the values of 0.034 (r_s = 1000 μm) and 0.0074 (r_s = 50 μm)

501   in July 1710. The averaged albedo reduction for the overall period of 1650-2014 is 0.0031 (r_s = 1000 μm) and 0.0007 (r_s = 50

502   μm) for clear conditions, and 0.0054 (r_s = 1000 μm) and 0.0011 (r_s = 50 μm) for cloudy conditions. During the anthropogenic
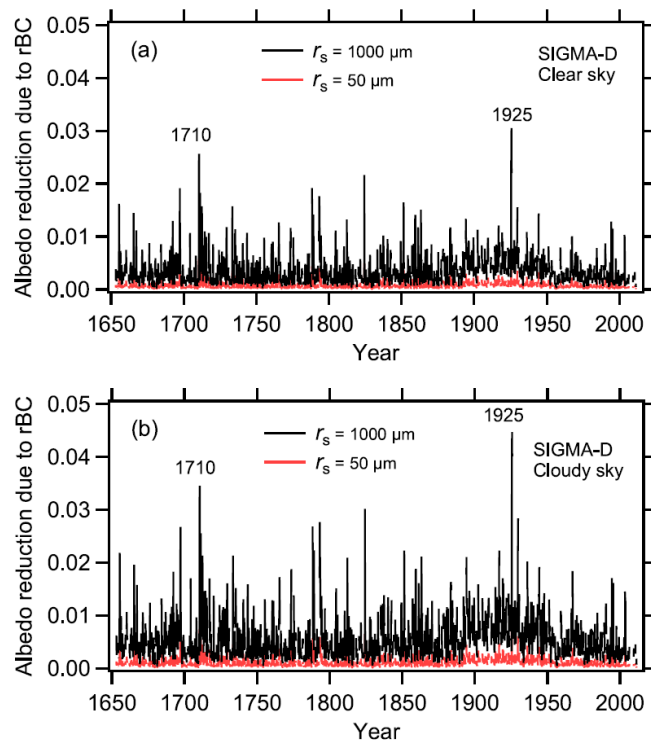
Figure 17: Temporal variation of albedo reduction for (a) clear sky and (b) cloudy sky conditions, calculated from monthly mean rBC mass concentrations, for two effective snow grain radii: r_s = 50 μm (representing new snow, indicated by the red line) and r_s = 1000 μm (indicating old melting snow, shown by the black line). The albedo reduction values are calculated for solar zenith angle at local solar noon on the 15th of each month, excluding the polar night period from November to February. The maximum albedo reduction is simulated in 1925 and followed by 1710.

503   concentration peak period of 1913-1933, the average albedo reduction increases to 0.0056 (r_s = 1000 µm) and 0.0012 (r_s = 50

504   µm) for clear conditions, and 0.0089 (r_s = 1000 µm) and 0.0019 (r_s = 50 µm) for cloudy conditions.

505   Warren (2019) described that an rBC concentration of 20 parts per billion in weight can cause broadband snow albedo

506   reductions of 1-2%. They also noted that for a typical daily average solar irradiance of 400 W m^{-2} in the Arctic during late

507   spring and early summer, a 1% albedo reduction can lead to a positive forcing of 4 W m^{-2} locally, similar to the forcing caused

508   by doubling CO_2. Our calculation results indicate that a 1% of reduction in albedo can occur at numerous local spike-like peaks

509   for r_s = 1000 µm including the recent several decades after 1950. During the anthropogenic concentration peak period (1913-

510   1933), the average albedo reduction approaches 1% (0.0089) for r_s = 1000 µm under cloudy sky conditions. Consequently, our

511   simulations suggest that the amount of albedo reduction remains relatively small as long as new snow conditions are maintained.

512   However, if the surface snow grains reach the size of old melting snow, which would have occurred during summer months at

513   the SIGMA-D site, the extent of albedo reduction becomes non-negligible.

514

515   **4 Conclusions**

516   We analysed the record of rBC over the past 350 years in the SIGMA-D ice core, which was drilled in northwest Greenland.

517   The improved technique for rBC measurement (Mori et al., 2016) and the CFA system built at NIPR allowed us to reconstruct

518   high temporal resolution records of the sizes and concentrations of rBC particles. Notably, this study marks the first

519   reconstruction of temporal changes in rBC size since the pre-industrial period.

520   The number and mass concentrations of rBC started to increase in the 1870s owing to anthropogenic input. The

521   concentrations reached their maxima in the 1910s–1920s, following which they decreased. By the 1960s, rBC concentrations

522   had reduced to levels close to or lower than those of the pre-industrial period. The trend of anthropogenic rBC at the SIGMA-

523   D site was generally similar to that reported previously for other ice core sites in Greenland, albeit with slight differences.

524   Backward trajectory analyses suggest that the major anthropogenic emission source that affected the SIGMA-D site was NA.

525   However, the backward trajectory analyses did not clearly explain the slight difference in the temporal trends of rBC between

526   the SIGMA-D site and the more southerly site D4. Anthropogenic rBC was transported to the SIGMA-D site mainly in the

527   winter half of the year, which was deduced by the changes in the seasonality of rBC concentrations. The backward trajectory

528   analyses produced consistent results, showing greater contributions from air masses from the industrial regions in NA, EUR,

529   and RUS in winter.

530   Pre-industrial rBC concentrations peaked in summer. In association with increased anthropogenic input,

531   concentrations increased in winter to early spring, which shifted the annual peak in concentration to winter–early spring. When

532   the anthropogenic input started to decline in the 1930s, concentrations in winter–early spring also decreased, which changed

533   the seasonality of rBC concentrations; by the 1990s, rBC concentrations peaked in summer once again. This suggests that the

534   major sources of rBC in recent years were not anthropogenic emissions but biomass burning. At the SIGMA-D site, rBC

535   originated from anthropogenic emissions made only a minor contribution to the rBC concentrations in the summer months

536   throughout the past 350 years. This enabled us to examine the temporal variability in biomass burning throughout the past 350

537   years, especially after the increase in anthropogenically derived rBC, which is a topic that has not been addressed by previous

538   studies on rBC data from other ice cores in the Arctic.

539   The size distributions of rBC particles have also changed owing to anthropogenic impact. The seasonality of MMD

540   and mBC also changed, associated with the concentration changes. Winter and summer mBC started to increase in the 1820s-

541   1830s, peaked in the 1890s–1930s when rBC concentrations peaked, and started to declinesince the 1930s. The winter and

542   summer MMD started to increase in the 1840s and 1810s, respectively, with larger rate of increase for winter MMD. While

543   winter MMD started to decrease in the 1900s – 1920s and has continued to decrease, the summer MMD did not exhibit a clear

544   downward trend. Increases in winter MMD and mBC associated with the increase in winter rBC concentrations suggest that

545   the diameter of rBC particles deposited over northwest Greenland were generally larger for anthropogenic rBC than for

546   biomass burning rBC. In contrast to rBC concentrations, neither MMD nor mBC returned to their pre-industrial values; instead,

547   they remained at higher values in the 1960s–2000s.

548   Pre-industrial rBC would have originated mainly from biomass burning. During the winters (December–February) of

549   the pre-industrial period, decadal averages of monthly mean mass and number concentrations were stable, and the sizes of rBC

550   particles were smaller than those in summer. This indicates that rBC in pre-industrial winters originated from biomass burning

551   in low latitudes where there was no snow cover in winter, and that biomass burning in low latitudes that affected Greenland

552   showed little change during the pre-industrial period. After the inflow of anthropogenic rBC started, it became difficult to

553   distinguish biomass burning rBC from anthropogenic rBC in winter, making it difficult to discuss the temporal changes in rBC

554   originated from low-latitude biomass burning in winter. However, we could discuss the temporal changes in boreal forest fires

555   that occur mainly in summer, the season with minimal anthropogenic input.

556   Sources of pre-industrial rBC were likely boreal forest fires primarily in NA. We investigated the temporal trend in

557   the decadal frequency of large boreal forest fire events using high summer peaks of number and mass concentrations of rBC.

558   We found no obvious trend of increase in the decadal frequency of large boreal forest fires until the decade of 1993–2002.

559   Furthermore, we found no trends of increase in the decadal averages of monthly mean mass and number concentrations in

560   summer during the past 350 years; we even found a trend of decrease for number concentrations. Although recent large fire

561   events in NA are attributed to global warming (Brown et al., 2023), the effects of global warming do not seem to have left

562   clear imprint in Greenland until the early 2000s. Therefore, we need further investigations using more recent ice core records

563   of rBC.

564   We analysed the temporal variation of potential albedo reduction due to rBC at the SIGMA-D site during the past

565   350 years using a physically based snow albedo model. Albedo reductions under the assumption of new snow grain size

566   remained below 0.01, even at the peak rBC concentration in 1925. Conversely, under the assumption of old melting snow grain

567   size, the albedo reduction frequently exceeded 0.01. Our calculation results reveal that a 1% of reduction in albedo can occur

568   at numerous local spike-like peaks in the case of old melting snow, including the recent several decades after 1950. During the

569   peak period of anthropogenic concentrations (1913-1933), the averaged albedo reduction approaches 1% for old melting snow

570   cases. Consequently, our simulations suggest that the magnitude of albedo reduction remains relatively small as long as new

571   snow conditions are maintained. However, if the surface snow grains reach the size of old melting snow, the amount of albedo

572   reduction becomes non-negligible.

573   Our new high temporal resolution records of rBC concentrations and sizes could contribute to evaluation of the

574   impacts of both anthropogenically derived and biomass burning originated rBC on Earth's radiation budget, albedo, rBC–

575   cloud interactions, and therefore rBC–climate interactions. They could also contribute to validation of emission inventories,

576   and aerosol and climate models. High temporal resolution rBC data since 2002 are necessary to investigate the impact of global

577   warming on boreal forest fires. Furthermore, high temporal resolution records of rBC concentrations and sizes during the early

578   Holocene and the last interglacial period when it was warmer than the present day (NEEM community members, 2013; Vinther

579   et al., 2009) should be obtained for better projections of rBC–climate interactions in a future warming world.

580

32

Appendix A

Figure A1: Monthly snow height change observed with an automatic weather station (AWS) at the SIGMA-D site during the period May 2014 – September 2015 (Matoba et al., 2015). It appears that there was more precipitation in summer than in winter, which could introduce some bias in monthly dating of the SIGMA-D ice core. Although the AWS data indicated that precipitation occurred in all months (Fig. A2), there were a few months when snow height change was negative mainly owing to wind scouring. Moreover, the seasonal variation in precipitation seems to exhibit significant year-to-year variability. However, by averaging monthly mean concentrations over 10-20 years (Fig. 11), we can observe changes in the seasonality of rBC.
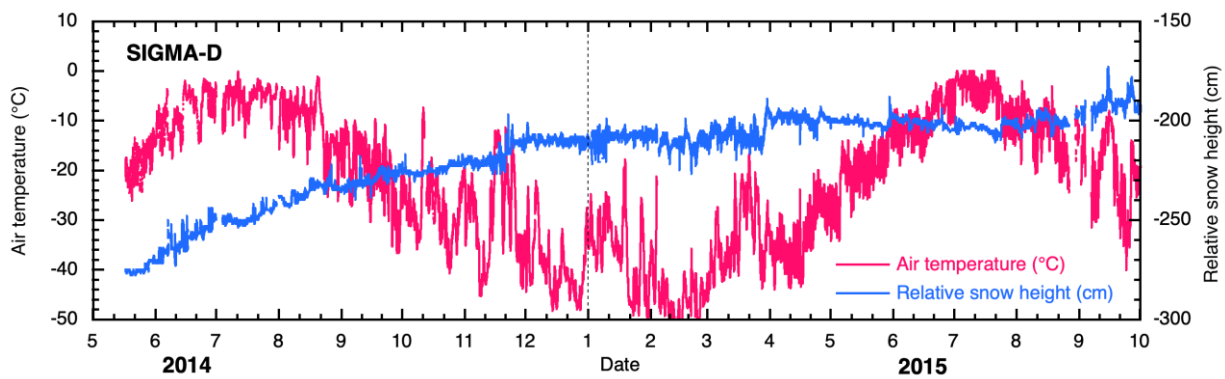

Figure A2. Seasonal variations of air temperature and relative snow height every 10 minutes observed at the SIGMA-D site during the period May 2014 – September 2015 (Matoba et al., 2015).
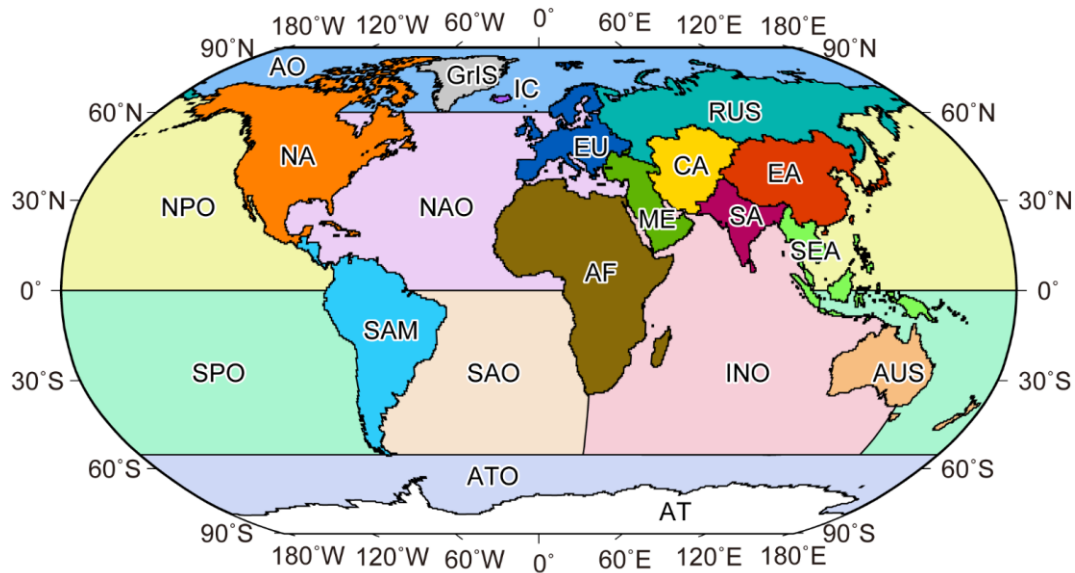
Figure A3: Map showing 21 regions used for calculating the regional contributions in backward trajectory analysis.

ME: Middle East, AT: Antarctica, AUS: Australia and New Zealand, SAM: South America, AF: Africa, EA: China and East Asia, EU: Europe, GrIS: Greenland Ice Sheet, SEA: Southeast Asia, SA: South Asia, CA: Central Asia, RUS: Russia, NA: North America, ATO: Antarctic Ocean, SPO: South Pacific Ocean, INO: Indian Ocean, NPO: North Pacific Ocean, SAO: South Atlantic Ocean, NAO: North Atlantic Ocean, AO: Arctic Ocean, IC: Iceland.
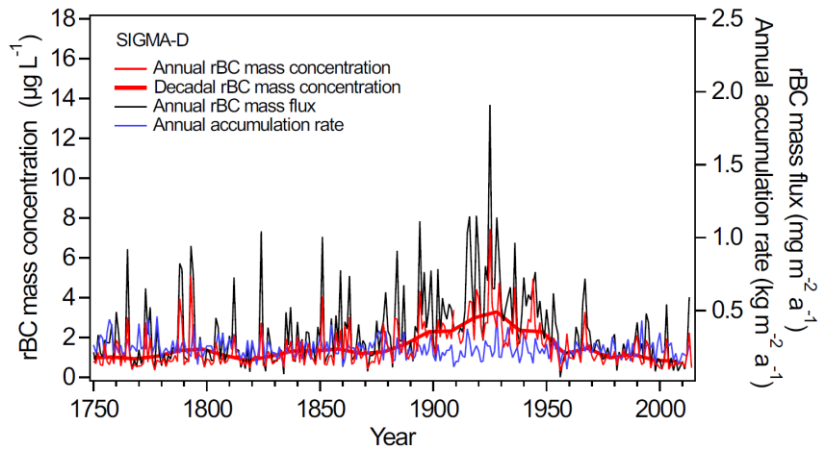
Figure A4: Annual mean and decadal mean rBC mass concentrations (thin and thick red curves, respectively), annual rBC mass flux (black), and annual accumulation rate (blue).
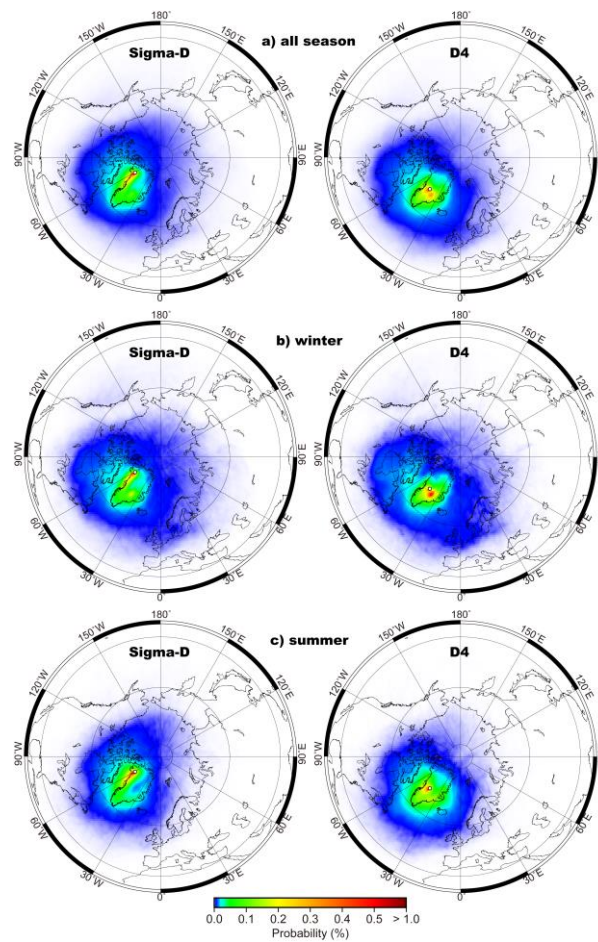
Figure A5: Probability distributions of air masses at (left) the SIGMA-D site and (right) the D4 site calculated without weighed with the local daily precipitation: (a) averages of all seasons, (b) averages of winter months (December-February), and (c) averages of summer months (May-July).

586

Table A1 Biomass burning events distinguished in the SIGMA-D ice core record, and in the records of other ice cores and surface snow from Greenland. Records from Greenland sites with temporal resolution of greater than 1 year were not used. Events distinguished in the SIGMA-D core were defined using rBC mass concentration peaks and NH_4^+ concentration peaks. For rBC, peaks exceeding the summer (May–July) averages + 2σ or 3σ were selected; for NH_4^+, peaks exceeding the annual average + 2σ or 3σ were selected. If a BC peak was found in April, August, or September, the year is written in parentheses. If an rBC or NH_4^+ summer peak in the SIGMA-D core with a concentration between the average + 1σ and 2σ was found in the same year when a large biomass burning event was recorded at other Greenland sites, the peak was also selected as a biomass burning event. If a year with a biomass burning event reported in previous studies agreed with that in the SIGMA-D core within 2 years, the records were considered to reflect the same event, and are written on the same line in the table.

A: Year of the event in the SIGMA-D core

B: Magnitude of the rBC mass concentration peak

C: Magnitude of the NH_4^+ concentration peak

D: Year of the event in ice cores and surface snow from Greenland sites other than the SIGMA-D site

E: Location of the ice core or surface snow in Greenland

F: Biomass burning proxies

G: References

604

SIGMA-D core (This study)			Ice cores and surface snow from Greenland sites other than the SIGMA-D site			
A	B	C	D	E	F	G
Year	Magnitude of rBC peak	Magnitude of NH_4^+ peak	Year	Location of ice core or surface snow	Proxy	Reference
1655	>average + 3σ	>average + 2σ	1654 1655	SUMMIT, NEEM SUMMIT	NH_4^+ NH_4^+, $HCOO^-$	(Legrand et al., 2016) (Savarino and Legrand, 1998)

1661	No data	>average + 2σ				
1665	>average + 3σ	>average + 2σ				
1667	>average + 2σ	>average + 1σ				
1675		>average + 3σ				
1684	>average + 1σ		1683	NEEM	NH_4^+	(Legrand et al., 2016)
1690		>average + 3σ				
1692	>average + 2σ					
1697	>average + 3σ	>average + 3σ	1699	SUMMIT	NH_4^+	(Legrand et al., 2016)
			1702–03	NEEM	NH_4^+	(Legrand et al., 2016)
			1702	NEEM	rBC	(Zennaro et al., 2014)
			1703	NEEM	rBC	(Zennaro et al., 2014)
1710	>average + 3σ	>average + 3σ				
1711	>average + 3σ	>average + 1σ				
1712	>average + 3σ	>average + 3σ				
1715	>average + 1σ	>average + 3σ				
1717	>average + 1σ	>average + 2σ	1719	NEEM	NH_4^+	(Legrand et al., 2016)
1724		>average + 2σ				
1727		>average + 3σ	1728	SUMMIT	NH_4^+	(Legrand et al., 2016)
1729	>average + 2σ					
1733	>average + 3σ		1732	NEEM	NH_4^+	(Legrand et al., 2016)
1735	>average + 2σ					
1740		>average + 3σ				
1743	>average + 1σ	>average + 2σ				
1750		>average + 3σ				
1756		>average + 3σ				
1761	>average + 1σ	>average + 3σ				

1765	>average + 2σ	>average + 2σ				
1773	>average + 1σ (>average + 3σ in September)	>average + 3σ	1771	NEEM	NH_4^+	(Legrand et al., 2016)
			1773	SUMMIT	NH_4^+	(Legrand et al., 2016)
			1773	SUMMIT	NH_4^+, $HCOO^-$	(Savarino and Legrand, 1998)
1775	>average + 1σ	>average + 2σ				
1788	>average + 3σ	>average + 3σ	1789	NEEM	rBC	(Zennaro et al., 2014)
1789	>average + 2σ (>average + 3σ in April)	>average + 3σ				
1793	>average + 3σ	>average + 3σ	1792	NEEM	NH_4^+	(Legrand et al., 2016)
1794	>average + 1σ	>average + 2σ	1794–95	SUMMIT	NH_4^+	(Legrand et al., 2016)
			1795	SUMMIT	NH_4^+, $HCOO^-$	(Legrand and De Angelis, 1996)
			1795	D4	NH_4^+	(Legrand et al., 2016)
1804	>average + 2σ	>average + 1σ				
1807		>average + 1σ	1807	SUMMIT, NEEM, D4	NH_4^+	(Legrand et al., 2016) (Legrand et al., 2016)
(1812)	(>average + 3σ in April)					
1824	>average + 3σ	>average + 2σ				
1827		>average + 2σ				
1835	>average + 1σ	>average + 3σ	1837	SUMMIT, NEEM, D4	NH_4^+ NH_4^+	(Legrand et al., 2016) (Legrand et al., 2016)
1840	>average + 1σ	No data	1839	SUMMIT	NH_4^+	(Legrand et al., 2016)
				SUMMIT	NH_4^+, $HCOO$	(Legrand and De Angelis, 1996)

			1846	SUMMIT	NH_4^+	(Legrand et al., 2016)
1849	>average + 1σ	No data	1847	D4	NH_4^+	(Legrand et al., 2016)
			1848	NEEM	NH_4^+	(Legrand et al., 2016)
1851	>average + 3σ	No data	1853	NEEM	NH_4^+	(Legrand et al., 2016)
		No data	1854	SUMMIT, D4	NH_4^+	(Legrand et al., 2016)
1859	>average + 3σ					
1861	>average + 2σ	>average + 1σ				
1863	>average + 3σ	No data	1863	SUMMIT, NEEM, D4	NH_4^+	(Legrand et al., 2016)
					NH_4^+	(Legrand et al., 2016)
				SUMMIT	NH_4^+, $HCOO^-$	(Savarino and Legrand, 1998)
		No data	1868	SUMMIT	NH_4^+	(Keegan et al., 2014)
			1869	D4	NH_4^+	(Legrand et al., 2016)
	No data	No data	1871	SUMMIT	NH_4^+	(Legrand et al., 2016)
			1872, D4	NEEM	NH_4^+	(Legrand et al., 2016)
1883	>average + 2σ	No data				
		No data	1886	SUMMIT, NEEM, D4	NH_4^+	(Legrand et al., 2016)
					NH_4^+	(Legrand et al., 2016)
				20D (Dye-3), GISP2 (SUMMIT)	NH_4^+	(Whitlow et al., 1994)
						(Legrand et al., 2016)
			1888	NEEM	NH_4^+	
		No data	1889	SUMMIT	rBC, NH_4^+	(Keegan et al., 2014)
				D4	NH_4^+	(Legrand et al., 2016)
			1890	SUMMIT	NH_4^+	(Legrand et al., 2016)

1894	>average + 1σ (>average + 3σ in April)	No data	1894–95 1894–95 1895	SUMMIT, NEEM, D4 SUMMIT	NH_4^+ NH_4^+ NH_4^+, $HCOO^-$	(Legrand et al., 2016) (Legrand et al., 2016) (Legrand and De Angelis, 1996)
1896	>average + 1σ	No data	1896	SUMMIT	NH_4^+, $HCOO^-$	(Savarino and Legrand, 1998)
1902	>average + 2σ	No data				
1909	>average + 1σ	No data	1908	SUMMIT, D4 SUMMIT SUMMIT	NH_4^+ NH_4^+, $HCOO^-$ rBC, NH_4^+	(Legrand et al., 2016) (Savarino and Legrand, 1998) (Keegan et al., 2014)
		No data	1921	NEEM	NH_4^+	(Legrand et al., 2016)
1925	>average + 3σ	No data	1923	SUMMIT, D4	NH_4^+	(Legrand et al., 2016)
1927	>average + 1σ	No data	1927–28	NEEM	NH_4^+	(Legrand et al., 2016)
(1929)	(>average + 3σ in September & October)		1929	SUMMIT, D4	NH_4^+	(Legrand et al., 2016)
1936	>average + 1σ	No data	1936–38 1938	SUMMIT SUMMIT, NEEM, D4	NH_4^+ NH_4^+	(Legrand et al., 2016) (Legrand et al., 2016)
1940	>average + 1σ	No data				
1944	>average + 3σ	No data	1942	NEEM, D4	NH_4^+	(Legrand et al., 2016)
		No data	1950	SUMMIT, NEEM, D4 SUMMIT	NH_4^+ NH_4^+, $HCOO^-$	(Legrand et al., 2016) (Savarino and Legrand, 1998)

		No data	1961	SUMMIT, NEEM, D4	NH_4^+	(Legrand et al., 2016)
				SUMMIT	NH_4^+, $HCOO^-$	(Savarino and Legrand, 1998)
				SE-Dome	Levoglucosan	(Parvin et al., 2019)
		No data	1964	SE-Dome	Levoglucosan	(Parvin et al., 2019)
		No data	1972	NEEM	rBC	(Zennaro et al., 2014)
			1973	NEEM	NH_4^+	(Legrand et al., 2016)
			1980	SUMMIT, NEEM, D4	NH_4^+	
1994	>average + 2σ	No data	1994	SE-Dome	Levoglucosan	(Parvin et al., 2019)
				SUMMIT	Levoglucosan, NH_4^+, $HCOO^-$, CH_3COO^-, $(C_2H_2O_4)^{2-}$	(Kehrwald et al., 2012; Dibb et al., 1996)
1995	>average + 2σ	No data				
		No data	1998	SE-Dome	Levoglucosan	(Parvin et al., 2019)
	No CFA data	No data	2012	SUMMIT	rBC, NH_4	(Keegan et al., 2014)
	No CFA data	No data	2013	SE-Dome	Levoglucosan	(Parvin et al., 2019)

605

606

Appendix B: Wet deposition vs dry deposition

We anticipate that the contribution of wet deposition was greater than that of dry deposition. It is difficult to estimate the wet and dry deposition ratio directly since there are no observations at the SIGMA-D site, as at most of the sites in the Arctic. Instead, we estimated the terminal velocity (V) of rBC particles falling onto the SIGMA-D site using the equation $V=2\rho r^2 g/9\zeta$ assuming spherical rBC particles. Here ρ, r, g, and ζ denote the density of rBC particles, the radius

of rBC particles, the acceleration of gravity, and the viscosity coefficient of the atmosphere, respectively. We used the

values 1800 kg m^{-3} and 1 μm for ρ and 2r (diameter), respectively. Assuming an atmospheric temperature of -40°C, ζ

was calculated to be 1.5×10^{-5} N s m^{-2}. With these values, the terminal velocity was estimated to be 6 m day^{-1}. Given that

the rBC particles fall from 500 m above the ice sheet surface at the SIGMA-D site, it would take approximately 100 days

for the rBC particles to reach the ice sheet surface, indicating a very small dry deposition velocity at the SIGMA-D site.

A study using the GEOS-Chem global chemical transport model (Breider et al., JGR, 2014) also indicated that the annual

mean fraction of dry deposition in the Arctic was only 11 %. Furthermore, Sinha et al. (JGR, 2018) showed that the dry

deposition was a small contributor (less than the uncertainties of the measurements, which were about 20%) to the total

rBC deposition at Ny-Ålesund, Svalbard, where the total water equivalent snowfall amount during September-April was

similar to the annual accumulation rate at the SIGMA-D site. Thus, it is reasonable to assume that the contribution of

dry deposition is small.

Data availability

All the data used in this study will be submitted to the Arctic Data Archive System (ADS) as soon as the manuscript has been

published.

Author contributions

KGA designed the study and led the manuscript writing. YOT was responsible for the BC measurements. YOT, MH, RD, and

JO performed the CFA analyses of the SIGMA-D core. MH and SM measured the ion concentrations in the discrete samples.

KoF, SM, AT, and NN dated the SIGMA-D ice core. MK calculated annual accumulation rates. KGA, YOT, and KaF analysed

the CFA data. KGA, YOT, NM, TM, SO, YK, and MK interpreted the BC data. KoF performed backward trajectory analyses.

TA analysed the AWS data. SM examined the melt features in the SIGMA-D ice core. TA designed and led the ice coring

project at SIGMA-D. TA computed the impacts of BC on albedo. All the authors discussed the results.

Competing interests

The authors declare that they have no conflict of interest.

References

Aoki, T., Aoki, T., Fukabori, M., and Uchiyama, A.: Numerical Simulation of the Atmospheric Effects on Snow Albedo with a Multiple Scattering Radiative Transfer Model for the Atmosphere-Snow System, J. Meteorol. Soc. of Japan. Ser. II, 77, 595–614, doi:10.2151/jmsj1965.77.2_595, 1999.

Aoki, T., Kuchiki, K., Niwano, M., Kodama, Y., Hosaka, M., and Tanaka, T.: Physically based snow albedo model for calculating broadband albedos and the solar heating profile in snowpack for general circulation models, J. Geophys. Res. Atmos., 116, D11114, doi:10.1029/2010JD015507, 2011.

Bauer, S. E., Bausch, A., Nazarenko, L., Tsigaridis, K., Xu, B., Edwards, R., Bisiaux, M., and McConnell, J.: Historical and future black carbon deposition on the three ice caps: Ice core measurements and model simulations from 1850 to 2100, J. Geophys. Res.-Atmos., 118, 7948–7961, doi:10.1002/jgrd.50612, 2013.

Baumgardner, D., Kok, G., and Raga, G.: Warming of the Arctic lower stratosphere by light absorbing particles, Geophys. Res. Lett., 31, https://doi.org/10.1029/2003GL018883, 2004.

Bisiaux, M. M., Edwards, R., McConnell, J. R., Albert, M. R., Anschütz, H., Neumann, T. A., Isaksson, E., and Penner, J. E.: Variability of black carbon deposition to the East Antarctic Plateau, 1800–2000 AD, Atmos. Chem. Phys., 12, 3799–3808, 10.5194/acp-12-3799-2012, 2012a.

663   Bisiaux, M. M., Edwards, R., McConnell, J. R., Curran, M. A. J., Van Ommen, T. D., Smith, A. M., Neumann, T. A., Pasteris,

664   D. R., Penner, J. E., and Taylor, K.: Changes in black carbon deposition to Antarctica from two high-resolution ice core

665   records, 1850–2000 AD, Atmos. Chem. Phys., 12, 4107–4115, 10.5194/acp-12-4107-2012, 2012b.

666   Bond, T. C., Doherty, S. J., Fahey, D. W., Forster, P. M., Berntsen, T., DeAngelo, B. J., Flanner, M. G., Ghan, S., Kärcher, B.,

667   Koch, D., Kinne, S., Kondo, Y., Quinn, P. K., Sarofim, M. C., Schultz, M. G., Schulz, M., Venkataraman, C., Zhang, H.,

668   Zhang, S., Bellouin, N., Guttikunda, S. K., Hopke, P. K., Jacobson, M. Z., Kaiser, J. W., Klimont, Z., Lohmann, U., Schwarz,

669   J. P., Shindell, D., Storelvmo, T., Warren, S. G., and Zender, C. S.: Bounding the role of black carbon in the climate system:

670   A scientific assessment, J. Geophys. Res.-Atmos. n/a-n/a, 10.1002/jgrd.50171, 2013.

671   Breider, T. J., Mickley, L. J., Jacob, D. J., Ge, C., Wang, J., Payer Sulprizio, M., Croft, B., Ridley, D. A., McConnell, J. R.,

672   Sharma, S., Husain, L., Dutkiewicz, V. A., Eleftheriadis, K., Skov, H., and Hopke, P. K.: Multidecadal trends in aerosol

673   radiative forcing over the Arctic: Contribution of changes in anthropogenic aerosol to Arctic warming since 1980, J.

674   Geophys. Res.-Atmos., 10.1002/2016JD025321, 2017.

675   Brown, P. T., Hanley, H., Mahesh, A., Reed, C., Strenfel, S. J., Davis, S. J., Kochanski, A. K., and Clements, C. B.: Climate

676   warming increases extreme daily wildfire growth risk in California, Nature, 621, 760–766, 10.1038/s41586-023-06444-3,

677   2023.

678   Calkin, D. E., Barrett, K., Cohen, J. D., Finney, M. A., Pyne, S. J., and Quarles, S. L.: Wildland-urban fire disasters aren't

679   actually a wildfire problem, P. Natl. Acad. Sci., 120, e2315797120, doi:10.1073/pnas.2315797120, 2023.

680   de la Casa, A. and Nasello, O.: Breakpoints in annual rainfall trends in Córdoba, Argentina、Atmos, Res., 95, 419−417,

681   2010.

682   Dibb, J. E., Talbot, R. W., Whitlow, S. I., Shipham, M. C., Winterle, J., McConnell, J., and Bales, R.: Biomass burning

683   signatures in the atmosphere and snow at Summit, Greenland: An event on 5 August 1994, Atmos. Environ., 30, 553–561,

684   10.1016/1352-2310(95)00328-2, 1996.

685   Du, Z.-H., Xiao, C.-D., Dou, T.-F., Li, C.-J., Ding, M.-H., Sharma, S., Ma, X.-Y., Wang, S.-M., and Zhang, W.-B.: A shallow

686   ice core from East Greenland showing a reduction in black carbon during 1990–2016, Adv. Clim. Change Res., 11, 360–

687   369, https://doi.org/10.1016/j.accre.2020.11.009, 2020.

688   Eckhardt, S., Pisso, I., Evangeliou, N., Zwaaftink, C. G., Plach, A., McConnell, J. R., Sigl, M., Ruppel, M., Zdanowicz, C.,

689   Lim, S., Chellman, N., Opel, T., Meyer, H., Steffensen, J. P., Schwikowski, M., and Stohl, A.: Revised historical Northern

44

690   Hemisphere black carbon emissions based on inverse modeling of ice core records, Nat. Commun., 14, 271,

691   10.1038/s41467-022-35660-0, 2023.

692 Fierz, C., Armstrong, R.L., Durand, Y., Etchevers, P., Greene, E., McClung, D.M., Nishimura, K., Satyawali, P.K. and

693   Sokratov, S.A.: The International Classification for Seasonal Snow on the Ground, IHP-VII Technical Documents in

694   Hydrology N°83, IACS Contribution N°1, UNESCO-IHP, Paris, 2009.

695 Fischer, H., Schupbach, S., Gfeller, G., Bigler, M., Rothlisberger, R., Erhardt, T., Stocker, T. F., Mulvaney, R., and Wolff, E.

696   W.: Millennial changes in North American wildfire and soil activity over the last glacial cycle, Nature Geosci., 8, 723–727,

697   doi:10.1038/ngeo2495, 2015.

698 Flanner, M. G., Zender, C. S., Randerson, J. T., and Rasch, P. J.: Present-day climate forcing and response from black carbon

699   in snow, J. Geophys. Res. 112, doi:10.1029/2006JD008003, 2007.

700 Gong, S. L., Zhao, T. L., Sharma, S., Toom-Sauntry, D., Lavoué, D., Zhang, X. B., Leaitch, W. R., and Barrie, L. A.:

701   Identification of trends and interannual variability of sulfate and black carbon in the Canadian High Arctic: 1981–2007, J.

702   Geophys. Res.-Atmos., 115, https://doi.org/10.1029/2009JD012943, 2010.

703 Goto-Azuma, K. and Koerner, R. M.: Ice core studies of anthropogenic sulfate and nitrate trends in the Arctic, J. Geophys.

704   Res.-Atmos., 106, 4959–4969, 2001.

705 Goto-Azuma, K., Dallmayr, R., Ogawa-Tsukagawa, Y., Moteki, N., Mori, T., Ohata, S., Kondo, Y., Koike, M., Hirabayashi,

706   M., Ogata, J., Kitamura, K., Kawamura, K., Fujita, K., Matoba, S., Nagatsuka, N., Tsushima, A., Fukuda, K., and Aoki, T.:

707   Technical note: High-resolution analyses of concentrations and sizes of black carbon particles deposited on northwest

708   Greenland over the past 350 years – Part 1. Continuous flow analysis of the SIGMA-D ice core using a Wide-Range Single-

709   Particle Soot Photometer and a high-efficiency nebulizer, accepted by Atmos. Phys. Chem.

710 Grieman, M. M., Aydin, M., Fritzsche, D., McConnell, J. R., Opel, T., Sigl, M., and Saltzman, E. S.: Aromatic acids in a

711   Eurasian Arctic ice core: a 2600-year proxy record of biomass burning, Clim. Past, 13, 395–410, 10.5194/cp-13-395-2017,

712   2017.

713 Grieman, M. M., Aydin, M., McConnell, J. R., and Saltzman, E. S.: Burning-derived vanillic acid in an Arctic ice core from

714   Tunu, northeastern Greenland, Clim. Past, 14, 1625–1637, 10.5194/cp-14-1625-2018, 2018.

715 Hanes, C. C., Wang, X., Jain, P., Parisien, M.-A., Little, J. M., and Flannigan, M. D.: Fire-regime changes in Canada over the

716   last half century, Can. J. Forest Res., 49, 256–269, 10.1139/cjfr-2018-0293, 2018.

717 Hennigan, C. J., Sullivan, A. P., Collett Jr., J. L., and Robinson, A. L.: Levoglucosan stability in biomass burning particles

718   exposed to hydroxyl radicals, Geophys. Res. Lett., 37, https://doi.org/10.1029/2010GL043088, 2010.

719 Hersbach, H., Bell, B., Berrisford, P., Hirahara, S., Horányi, A., Muñoz-Sabater, J., Nicolas, J., Peubey, C., Radu, R., Schepers,

720   D., Simmons, A., Soci, C., Abdalla, S., Abellan, X., Balsamo, G., Bechtold, P., Biavati, G., Bidlot, J., Bonavita, M., De

721   Chiara, G., Dahlgren, P., Dee, D., Diamantakis, M., Dragani, R., Flemming, J., Forbes, R., Fuentes, M., Geer, A.,

722   Haimberger, L., Healy, S., Hogan, R. J., Hólm, E., Janisková, M., Keeley, S., Laloyaux, P., Lopez, P., Lupu, C., Radnoti,

723   G., de Rosnay, P., Rozum, I., Vamborg, F., Villaume, S., and Thépaut, J.-N.: The ERA5 global reanalysis, Q. J. Roy. Meteor.

724   Soc., 146, 1999–2049, https://doi.org/10.1002/qj.3803, 2020.

725 Hoesly, R. M., Smith, S. J., Feng, L., Klimont, Z., Janssens-Maenhout, G., Pitkanen, T., Seibert, J. J., Vu, L., Andres, R. J.,

726   Bolt, R. M., Bond, T. C., Dawidowski, L., Kholod, N., Kurokawa, J. I., Li, M., Liu, L., Lu, Z., Moura, M. C. P., O'Rourke,

727   P. R., and Zhang, Q.: Historical (1750–2014) anthropogenic emissions of reactive gases and aerosols from the Community

728   Emissions Data System (CEDS), Geosci. Model Dev., 11, 369–408, 10.5194/gmd-11-369-2018, 2018.

729 Jurányi, Z., Zanatta, M., Lund, M. T., Samset, B. H., Skeie, R. B., Sharma, S., Wendisch, M., and Herber, A.: Atmospheric

730   concentrations of black carbon are substantially higher in spring than summer in the Arctic, Comm. Earth Environ., 4, 91,

731   10.1038/s43247-023-00749-x, 2023.

732 Kaspari, S. D., Schwikowski, M., Gysel, M., Flanner, M. G., Kang, S., Hou, S., and Mayewski, P. A.: Recent increase in black

733   carbon concentrations from a Mt. Everest ice core spanning 1860–2000 AD, Geophys. Res. Lett., 38, L04703,

734   10.1029/2010gl046096, 2011.

735 Kawamura, K., Izawa, Y., Mochida, M., and Shiraiwa, T.: Ice core records of biomass burning tracers (levoglucosan and

736   dehydroabietic, vanillic and p-hydroxybenzoic acids) and total organic carbon for past 300 years in the Kamchatka

737   Peninsula, Northeast Asia, Geochim. Cosmoshim. Acta, 99, https://doi.org/10.1016/j.gca.2012.08.006 317-329, 2012.

738 Keane, R. E., Agee, J. K., Fulé, P., Keeley, J. E., Key, C., Kitchen, S. G., Miller, R., and Schulte, L. A.: Ecological effects of

739   large fires on US landscapes: benefit or catastrophe? Int. J. Wildland Fire, 17, 696–712, https://doi.org/10.1071/WF07148,

740   2008.

741 Keegan, K. M., Albert, M. R., McConnell, J. R., and Baker, I.: Climate change and forest fires synergistically drive widespread

742   melt events of the Greenland Ice Sheet, P. Natl. Acad. Sci., 111, 7964–7967, 10.1073/pnas.1405397111, 2014.

743 Keeley, J. E. and Syphard, A. D.: Large California wildfires: 2020 fires in historical context, Fire Ecology, 17, 22,

744   10.1186/s42408-021-00110-7, 2021.

745 Kehrwald, N., Zangrando, R., Gabrielli, P., Jaffrezo, J.-L., Boutron, C., Barbante, C., and Gambaro, A.: Levoglucosan as a

746   specific marker of fire events in Greenland snow, Tellus B: Chem. Phys. Meteorol., 64, 18196, 10.3402/tellusb.v64i0.18196,

747   2012.

748 Lamarque, J. F., Bond, T. C., Eyring, V., Granier, C., Heil, A., Klimont, Z., Lee, D., Liousse, C., Mieville, A., Owen, B.,

749   Schultz, M. G., Shindell, D., Smith, S. J., Stehfest, E., Van Aardenne, J., Cooper, O. R., Kainuma, M., Mahowald, N.,

750   McConnell, J. R., Naik, V., Riahi, K., and van Vuuren, D. P.: Historical (1850–2000) gridded anthropogenic and biomass

751   burning emissions of reactive gases and aerosols: methodology and application, Atmos. Chem. Phys., 10, 7017–7039,

752   10.5194/acp-10-7017-2010, 2010.

753 Legrand, M. and De Angelis, M.: Light carboxylic acids in Greenland ice: A record of past forest fires and vegetation emissions

754   from the boreal zone, J. Geophys. Res.-Atmos., 101, 4129–4145, https://doi.org/10.1029/95JD03296, 1996.

755 Legrand, M. and Mayewski, P.: Glaciochemistry of polar ice cores: A review, Rev. Geophys., 35, 219–243,

756   10.1029/96RG03527, 1997.

757 Legrand, M., De Angelis, M., Staffelbach, T, Neftel, A., and Stauffer, B.: Large perturbations of ammonium and organic acids

758   in the Summit-Greenland ice core. Fingerprint from forest fires? Geophys. Res. Lett., 19, 473-475,

759   http://dx.doi.org/10.1029/91GL03121, 1992.

760 Legrand, M., McConnell, J., Fischer, H., Wolff, E. W., Preunkert, S., Arienzo, M., Chellman, N., Leuenberger, D., Maselli,

761   O., Place, P., Sigl, M., Schüpbach, S., and Flannigan, M.: Boreal fire records in Northern Hemisphere ice cores: A review,

762   Clim. Past, 12, 2033–2059, 10.5194/cp-12-2033-2016, 2016.

763 Lim, S., Faïn, X., Zanatta, M., Cozic, J., Jaffrezo, J.-L., Ginot, P., and Laj, P.: Refractory black carbon mass concentrations

764   in snow and ice: method evaluation and inter-comparison with elemental carbon measurement, Atmos. Meas. Tech., 7,

765   3307-3324. doi: 10.5194/amt-7-3307-2014, 2014.

766 Marlon, J. R., Bartlein, P. J., Gavin, D. G., Long, C. J., Anderson, R. S., Briles, C. E., Brown, K. J., Colombaroli, D., Hallett,

767   D. J., Power, M. J., Scharf, E. A., and Walsh, M. K.: Long-term perspective on wildfires in the western USA, P. Natl. Acad.

768   Sci., 109, E535–E543, 10.1073/pnas.1112839109, 2012.

Marlon, J. R., Bartlein, P. J., Daniau, A.-L., Harrison, S. P., Maezumi, S. Y., Power, M. J., Tinner, W., and Vanniére, B.: Global biomass burning: a synthesis and review of Holocene paleofire records and their controls, Quaternary Sci. Rev., 65, 5–25, http://dx.doi.org/10.1016/j.quascirev.2012.11.029, 2013.

Marlon, J. R., Kelly, R., Daniau, A. L., Vannière, B., Power, M. J., Bartlein, P., Higuera, P., Blarquez, O., Brewer, S., Brücher, T., Feurdean, A., Romera, G. G., Iglesias, V., Maezumi, S. Y., Magi, B., Courtney Mustaphi, C. J., and Zhihai, T.: Reconstructions of biomass burning from sediment-charcoal records to improve data–model comparisons, Biogeosciences, 13, 3225–3244, 10.5194/bg-13-3225-2016, 2016.

Massling, A., Nielsen, I. E., Kristensen, D., Christensen, J. H., Sørensen, L. L., Jensen, B., Nguyen, Q. T., Nøjgaard, J. K., Glasius, M., and Skov, H.: Atmospheric black carbon and sulfate concentrations in Northeast Greenland, Atmos. Chem. Phys., 15, 9681–9692, 10.5194/acp-15-9681-2015, 2015.

Matoba, S., Motoyama, H., Fujita, K., Yamasaki, T., Minowa, M., Onuma, Y., Komuro, Y., Aoki, T., Yamaguchi, S., Sugiyama, S., and Enomoto, H.: Glaciological and meteorological observations at the SIGMA-D site, northwestern Greenland Ice Sheet, B. Glaciol. Res., 33, 7–14, 10.5331/bgr.33.7, 2015.

Matsui, H., Mori, T., Ohata, S., Moteki, N., Oshima, N., Goto-Azuma, K., Koike, M., and Kondo, Y.: Contrasting source contributions of Arctic black carbon to atmospheric concentrations, deposition flux, and atmospheric and snow radiative effects, Atmos. Chem. Phys., 22, 8989–9009, 10.5194/acp-22-8989-2022, 2022.

McConnell, J. R.: New Directions: Historical black carbon and other ice core aerosol records in the Arctic for GCM evaluation, Atmos. Environ., 44, 2665–2666, https://doi.org/10.1016/j.atmosenv.2010.04.004, 2010.

McConnell, J. R., Edwards, R., Kok, G. L., Flanner, M. G., Zender, C. S., Saltzman, E. S., Banta, J. R., Pasteris, D. R., Carter, M. M., and Kahl, J. D.: 20th-century industrial black carbon emissions altered Arctic climate forcing, Science, 317, 1381–1384, 10.1126/science.1144856, 2007.

Mori, T., Moteki, N., Ohata, S., Koike, M., Goto-Azuma, K., Miyazaki, Y., and Kondo, Y.: Improved technique for measuring the size distribution of black carbon particles in liquid water, Aerosol Sci. Tech., 50, 242–254, 10.1080/02786826.2016.1147644, 2016.

Mori, T., Goto-Azuma, K., Kondo, Y., Ogawa-Tsukagawa, Y., Miura, K., Hirabayashi, M., Oshima, N., Koike, M., Kupiainen, K., Moteki, N., Ohata, S., Sinha, P. R., Sugiura, K., Aoki, T., Schneebeli, M., Steffen, K., Sato, A., Tsushima, A., Makarov,

795   V., Omiya, S., Sugimoto, A., Takano, S., and Nagatsuka, N.: Black Carbon and Inorganic Aerosols in Arctic Snowpack, J.

796   Geophys. Res.-Atmos., 124, 13325–13356, 10.1029/2019jd030623, 2019.

797 Moseid, K. O., Schulz, M., Eichler, A., Schwikowski, M., McConnell, J. R., Olivié, D., Criscitiello, A. S., Kreutz, K. J., and

798   Legrand, M.: Using ice cores to evaluate CMIP6 aerosol concentrations over the historical era, J. Geophys. Res.-Atmos.,

799   127, e2021JD036105, https://doi.org/10.1029/2021JD036105, 2022.

800 Mosher, B. W., Winkler, P., and Jaffrezo, J.-L.: Seasonal aerosol chemistry at Dye 3, Greenland, Atmos. Environ. A-Gen., 27,

801   2761–2772, https://doi.org/10.1016/0960-1686(93)90308-L, 1993.

802 Moteki, N.: Climate-relevant properties of black carbon aerosols revealed by in situ measurements: a review, Prog. Earth

803   Planet. Sci., 10, 12, 10.1186/s40645-023-00544-4, 2023.

804 Moteki, N. and Kondo, Y.: Dependence of laser-induced incandescence on physical properties of black carbon aerosols:

805   Measurements and theoretical interpretation, Aerosol Sci. Tech., 44, 663–675, 10.1080/02786826.2010.484450, 2010.

806 Muggeo, V. M. R.: Estimating regression models with unknown break-points, Stat. Med., 22, 3055–

807   3071, https://doi.org/10.1002/sim.1545, 2003.

808 Nagatsuka, N., Goto-Azuma, K., Tsushima, A., Fujita, K., Matoba, S., Onuma, Y., Dallmayr, R., Kadota, M., Hirabayashi, M.,

809   Ogata, J., Ogawa-Tsukagawa, Y., Kitamura, K., Minowa, M., Komuro, Y., Motoyama, H., and Aoki, T.: Variations in

810   mineralogy of dust in an ice core obtained from northwestern Greenland over the past 100 years, Clim. Past, 17, 1341–1362,

811   10.5194/cp-17-1341-2021, 2021.

812 NEEM Community Members: Eemian interglacial reconstructed from a Greenland folded ice core, Nature, 493, 489–494,

813   10.1038/nature11789, 2013.

814 Ohata, S., Moteki, N., Schwarz, J., Fahey, D., and Kondo, Y.: Evaluation of a method to measure black carbon particles

815   suspended in rainwater and snow samples, Aerosol Sci. Technol., 47, 1073–1082, 10.1080/02786826.2013.824067, 2013.

816 Osmont, D., Wendl, I. A., Schmidely, L., Sigl, M., Vega, C. P., Isaksson, E., and Schwikowski, M.: An 800-year high-

817   resolution black carbon ice core record from Lomonosovfonna, Svalbard, Atmos. Chem. Phys., 18, 12777–12795,

818   10.5194/acp-18-12777-2018, 2018.

819 Parvin, F., Seki, O., Fujita, K., Iizuka, Y., Matoba, S., Ando, T., and Sawada, K.: Assessment for paleoclimatic utility of

820   biomass burning tracers in SE-Dome ice core, Greenland, Atmos. Environ., 196, 86–94,

821   https://doi.org/10.1016/j.atmosenv.2018.10.012, 2019.

822 Petzold, A., Ogren, J. A., Fiebig, M., Laj, P., Li, S.-M., Baltensperger6, U., Holzer-Popp, T., Kinne, S., Pappalardo, G.,

823 Sugimoto, N., Wehrli, C., Wiedensohler, A., and Zhang, X.-Y.: Recommendations for reporting "black carbon"

824 measurements, Atmos. Chem. Phys., 13, 8365–8379, 10.5194/acp-13-8365-2013, 2013.

825 Pokhrel, A., Kawamura, K., Kunwar, B., Ono, K., Tsushima, A., Seki, O., Matoba, S., and Shiraiwa, T.: Ice core records of

826 levoglucosan and dehydroabietic and vanillic acids from Aurora Peak in Alaska since the 1660s: A proxy signal of biomass-

827 burning activities in the North Pacific Rim, Atmos. Chem. Phys., 20, 597–612, 10.5194/acp-20-597-2020, 2020.

828 Power, M. J., Marlon, J. R., Bartlein, P. J., and Harrison, S. P.: Fire history and the Global Charcoal Database: A new tool for

829 hypothesis testing and data exploration, Palaeogeogr. Palaeocl., 291, 52–59, http://dx.doi.org/10.1016/j.palaeo.2009.09.014,

830 2010.

831 Power, M., Mayle, F., Bartlein, P., Marlon, J., Anderson, R., Behling, H., Brown, K., Carcaillet, C., Colombaroli, D., Gavin,

832 D., Hallett, D., Horn, S., Kennedy, L., Lane, C., Long, C., Moreno, P., Paitre, C., Robinson, G., Taylor, Z., and Walsh, M.:

833 Climatic control of the biomass-burning decline in the Americas after ad 1500, The Holocene, 23, 3–13,

834 10.1177/0959683612450196, 2013.

835 Qi, L. and Wang, S.: Sources of black carbon in the atmosphere and in snow in the Arctic, Sci. Total Environ., 691, 442–454,

836 https://doi.org/10.1016/j.scitotenv.2019.07.073, 2019.

837 Rantanen, M., Karpechko, A. Y., Lipponen, A., Nordling, K., Hyvärinen, O., Ruosteenoja, K., Vihma, T., and Laaksonen, A.:

838 The Arctic has warmed nearly four times faster than the globe since 1979, Comm. Earth Environ., 3, 168, 10.1038/s43247-

839 022-00498-3, 2022.

840 Rasmussen, S. O., Seierstad, I. K., Andersen, K. K., Bigler, M., Dahl-Jensen, D., and Johnsen, S. J.: Synchronization of the

841 NGRIP, GRIP, and GISP2 ice cores across MIS 2 and palaeoclimatic implications, Quaternary Sci. Rev., 27, 18–28,

842 http://dx.doi.org/10.1016/j.quascirev.2007.01.016, 2008.

843 Rubino, M., D'Onofrio, A., Seki, O., and Bendle, J. A.: Ice-core recodes of biomass burning, The Anthropocene Rev., 3, 140-

844 162, https://journals.sagepub.com/doi/abs/10.1177/2053019615605117, 2016.

845 Ruppel, M. M., Isaksson, I., Ström, J., Beaudon, E., Svensson, J., Pedersen,C. A., and Korhola, A.: Increase in elemental

846 carbon values between 1970 and 2004 observed in a 300-year ice core from Holtedahlfonna (Svalbard), Atmos. Chem. Phys.,

847 14, 11447–11460, 10.5194/acp-14-11447-2014, 2014.

848   Savarino, J. and Legrand, M.: High northern latitude forest fires and vegetation emissions over the last millennium inferred

849   from the chemistry of a central Greenland ice core, J. Geophys. Res.-Atmos., 103, 8267–8279, 10.1029/97jd03748, 1998.

850   Schmeisser, L., Backman, J., Ogren, J. A., Andrews, E., Asmi, E., Starkweather, S., Uttal, T., Fiebig, M., Sharma, S.,

851   Eleftheriadis, K., Vratolis, S., Bergin, M., Tunved, P., and Jefferson, A.: Seasonality of aerosol optical properties in the

852   Arctic, Atmos. Chem. Phys., 18, 11599–11622, 10.5194/acp-18-11599-2018, 2018.

853   Schwarz, J. P., Gao, R. S., Perring, A. E., Spackman, J. R., and Fahey, D. W.: Black carbon aerosol size in snow, Sci. Rep., 3,

854   1356, 10.1038/srep01356, 2013.

855   Sharma, S., Andrews, E., Barrie, L. A., Ogren, J. A., and Lavoué, D.: Variations and sources of the equivalent black carbon in

856   the high Arctic revealed by long-term observations at Alert and Barrow: 1989–2003, J. Geophys. Res.-Atmos., 111,

857   https://doi.org/10.1029/2005JD006581, 2006.

858   Sharma, S., Barrie, L. A., Magnusson, E., Brattström, G., Leaitch, W. R., Steffen, A., and Landsberger, S.: A factor and trends

859   analysis of multidecadal lower tropospheric observations of Arctic aerosol composition, black carbon, ozone, and mercury

860   at Alert, Canada, J. Geophys. Res.-Atmos., 124, 14133–14161, https://doi.org/10.1029/2019JD030844, 2019.

861   Sharma, S., Ishizawa, M., Chan, D., Lavoué, D., Andrews, E., Eleftheriadis, K., and Maksyutov, S.: 16-year simulation of

862   Arctic black carbon: Transport, source contribution, and sensitivity analysis on deposition, J. Geophys. Res.-Atmos., 118,

863   943–964, https://doi.org/10.1029/2012JD017774, 2013.

864   Shindell, D. and Faluvegi, G.: Climate response to regional radiative forcing during the twentieth century, Nat. Geosci., 2,

865   294–300, 10.1038/ngeo473, 2009.

866   Sinnl, G., Winstrup, M., Erhardt, T., Cook, E., Jensen, C. M., Svensson, A., Vinther, B. M., Muscheler, R., and Rasmussen, S.

867   O.: A multi-ice-core, annual-layer-counted Greenland ice-core chronology for the last 3800 years: GICC21, Clim. Past, 18,

868   1125–1150, 10.5194/cp-18-1125-2022, 2022.

869   Skakun, R. Whitman, E., Little, J. M., and Parisien, M.-A.: Area burned adjustments to historical wildfires in Canada, Environ.

870   Res. Lett. 16 064014, 2021.

871   Stein, A. F., Draxler, R. R., Rolph, G. D., Stunder, B. J. B., Cohen, M. D., and Ngan, F.: NOAA's HYSPLIT atmospheric

872   transport and dispersion modeling system, B. Am. Meteorol. Soc., 96, 2059–2077, https://doi.org/10.1175/BAMS-D-14-

873   00110.1, 2015.

874 Stephens, M., Turner, N., and Sandberg, J.: Particle identification by laser-induced incandescence in a solid-state laser cavity,

875   Appl. Opt., 42, 3726–3736, 10.1364/AO.42.003726, 2003.

876 van Marle, M. J. E., Kloster, S., Magi, B. I., Marlon, J. R., Daniau, A. L., Field, R. D., Arneth, A., Forrest, M., Hantson, S.,

877   Kehrwald, N. M., Knorr, W., Lasslop, G., Li, F., Mangeon, S., Yue, C., Kaiser, J. W., and van der Werf, G. R.: Historic

878   global biomass burning emissions for CMIP6 (BB4CMIP) based on merging satellite observations with proxies and fire

879   models (1750–2015), Geosci. Model Dev., 10, 3329–3357, 10.5194/gmd-10-3329-2017, 2017.

880 Vinther, B. M., Buchardt, S. L., Clausen, H. B., Dahl-Jensen, D., Johnsen, S. J., Fisher, D. A., Koerner, R. M., Raynaud, D.,

881   Lipenkov, V., Andersen, K. K., Blunier, T., Rasmussen, S. O., Steffensen, J. P., and Svensson, A. M.: Holocene thinning of

882   the Greenland ice sheet, Nature, 461, 385–388, 10.1038/nature08355, 2009.

883 Wang, M., Xu, B., Kaspari, S. D., Gleixner, G., Schwab, V. F., Zhao, H., Wang, H., and Yao, P.: Century-long record of black

884   carbon in an ice core from the Eastern Pamirs: Estimated contributions from biomass burning, Atmos. Environ., 115, 79–

885   88, https://doi.org/10.1016/j.atmosenv.2015.05.034, 2015.

886 Wang, D., Guan, D., Zhu, S., Kinnon, M. M., Geng, G., Zhang, Q., Zheng, H., Lei, T., Shao, S., Gong, P., and Davis, S. J.:

887   Economic footprint of California wildfires in 2018, Nat. Sustain., 4, 252–260, 10.1038/s41893-020-00646-7, 2021.

888 Warren, S. G.: Light-Absorbing Impurities in Snow: A Personal and Historical Account, Front. Earth Sci. 6:250. doi:

889   10.3389/feart.2018.00250, 2019.

890 Wendl, I. A., Menking, J. A., Färber, R., Gysel, M., Kaspari, S. D., Laborde, M. J. G., and Schwikowski, M.: Optimized

891   method for black carbon analysis in ice and snow using the Single Particle Soot Photometer, Atmos. Meas. Tech., 7, 2667–

892   2681, 10.5194/amt-7-2667-2014, 2014.

893 Whitlow, S., Mayewski, P., Dibb, J., Holdsworth, G., and Twickler, M.: An ice-core-based record of biomass burning in the

894   Arctic and Subarctic, 1750–1980, Tellus B, 46, 234–242, https://doi.org/10.1034/j.1600-0889.1994.t01-2-00006.x, 1994.

895 Whitman, E., Parisien, M.-A., Thompson, D. K., Hall, R. J., Skakun, R. S., and Flannigan, M. D.: Variability and drivers of

896   burn severity in the northwestern Canadian boreal forest, Ecosphere, 9, e02128, https://doi.org/10.1002/ecs2.2128, 2018.

897 Wiscombe, W. J. and Warren, S. G.: A model for the spectral albedo of snow. I: Pure snow, J. Atmos. Sci., 37, 2712–2733,

898   doi:10.1175/1520-0469(1980)037<2712:AMFTSA>2.0.CO;2, 1980.

899   Zdanowicz, C. M., Proemse, B. C., Edwards, R., Feiteng, W., Hogan, C. M., Kinnard, C., and Fisher, D.: Historical black

900   carbon deposition in the Canadian High Arctic: a 250-year long ice-core record from Devon Island, Atmos. Chem. Phys.,

901   18, 12345–12361, 10.5194/acp-18-12345-2018, 2018.

902   Zennaro, P., Kehrwald, N., McConnell, J. R., Schüpbach, S., Maselli, O. J., Marlon, J., Vallelonga, P., Leuenberger, D.,

903   Zangrando, R., Spolaor, A., Borrotti, M., Barbaro, E., Gambaro, A., and Barbante, C.: Fire in ice: two millennia of boreal

904   forest fire history from the Greenland NEEM ice core, Clim. Past, 10, 1905–1924, 10.5194/cp-10-1905-2014, 2014.

905